Florian Pilat, BSc

Fabrication and Analysis of Quantum Cascade Lasers for Microfluidic Applications

MASTER'S THESIS

to achieve the university degree of

Diplom-Ingenieur

Master's degree programme: Technical Physics

submitted to

Graz University of Technology

Supervisor

Peter Hadley, Univ.-Prof. Ph.D.
Institute of Solid State Physics
in cooperation with TU Wien

Graz, October 2020

AFFIDAVIT

I declare that I have authored this thesis independently, that I have not used other than the declared sources/resources, and that I have explicitly indicated all material which has been quoted either literally or by content from the sources used. The text document uploaded to TUGRAZonline is identical to the present master's thesis.

Date, Signature

Abstract

With the miniaturization of smart devices, a certain need for compact sensors emerged. Quantum cascade technology offers interesting concepts to address this issue in the field of chemical sensing. Molecules show very distinct and strong absorption features in the mid-infrared spectral region, making it quite appealing for sensing and spectroscopy applications. It is therefore often referred to as fingerprint region. Quantum cascade devices, namely lasers and detectors, are able to efficiently emit and detect light for that purpose. Moreover, it is possible to precisely tailor their operation wavelength to directly target an absorption feature of a molecule of interest. Another important aspect when it comes to miniaturization is the possibility to use an unbiased laser, if designed properly, as a detector for the same wavelength radiation, allowing for monolithic integration and lab-on-a-chip applications.

This thesis focuses on such quantum cascade laser detector devices and their implementation in a microfluidic sensor cell. Starting from device characterisation and development of the cell, stability and transient behaviour are investigated. Absorption spectroscopy experiments are conducted and lead to a solid framework for future investigations and diverse applications. Additionally, a sensor for in-situ measurements is developed and evaluated.

Kurzfassung

Mit der Miniaturisierung intelligenter Geräte gewann die Entwicklung kompakter Sensoren bedeutend an Relevanz. Die Quantenkaskadentechnologie bietet vielversprechende Konzepte für deren Realisierung im Bereich chemischer Messungen. Moleküle zeigen ein starkes und sehr spezifisches Absorptionsverhalten im mittleren Infrarotraum („fingerprint region"), wodurch sich dieser Frequenzbereich besonders für Messgeräte und Sensoren eignet. Quantenkaskadenlaser und -detektoren können effizient solche Strahlung aussenden bzw. detektieren. Deren Wellenlänge kann sogar individuell angepasst werden, um die Absorptionslinien eines bestimmten Moleküls zu adressieren. Ein weiterer wichtiger Aspekt im Sinne der Miniaturisierung ist die Möglichkeit einen entsprechend designten Laser, der nicht betrieben wird, als Detektor für Strahlung derselben Wellenlänge verwenden zu können. Dies ermöglicht monolithische Integration und „Lab-on-a-chip"-Anwendungen. Diese Arbeit beschäftigt sich mit solchen Quantenkaskadensensoren und deren Integrierung in eine mikrofluidische Messzelle. Die Geräte werden charakterisiert, eine Zelle entwickelt und Messungen von Stabilität und Einschwingverhalten werden durchgeführt. Mit dem fertigen Sensor wird Absorptionsspektroskopie betrieben und somit eine solide Basis für zukünftige Forschung und Anwendungen geschaffen. Zusätzlich wird das erlangte Wissen übertragen und ein in-situ-Sensor entwickelt und getestet.

Acknowledgements

First of all, I would like to thank my supervisors from TU Wien, Gottfried Strasser and Borislav Hinkov, for the opportunity to experience a state-of-the-art research environment in all its facets first-hand and for their guidance and insightful feedback. Also, I would like to say thank you to my supervisor from TU Graz, Peter Hadley, for his valuable inputs and support.

A big thanks goes to all the people at FKE and ZMNS. It was an inspiring time for me working amidst such gifted and passionate researchers, who made the CH-building a place I would always gladly go to. Thanks, Hedwig, for not only being my mentor in the cleanroom and the labs, but also for being a friend. Thanks, Johannes, for recruiting me and for fruitful discussions. Thanks, Nikola, for showing an experimentalist the beauty of theory. Thanks to Anna, Benedikt, Erich, Hanh, Hermann, Max, Max, Mauro, Miriam, Sandro, Suzy and Werner for all the scientific, but also non-scientific conversations.

I am very grateful to have studied with such a diverse bunch of young scientists, whom I have grown very fond of. Thanks, Fabian, Georg, Jakob, Julian, Markus, Pascal, Robert and Tobias for our time in Graz. Thanks, Fabian, Matzi, Thomas and Sven for the musical balance to studying. A special thanks goes to Clemens. You always made me feel welcome and appreciated, even in times I had low self-esteem. I will cherish our friendship in all the days to come.

I would not have been able to successfully finish my studies without the best WG one could wish for. Thanks, Berni, Conny, Diddi and Martin, for making Graz feel like home to me. I also wish to say thank you to Berni, whom I have known for ages, but only really got to know in Graz. Thanks for all the inspiring discussions and our culinary explorations.

Thanks, Alex, for being the amazing person you are to me and for supporting me the last couple of years in so many ways.

Molli, you have become a good friend over the last years and always had a sympathetic ear, when I needed someone to talk to. I am grateful to have you in my life.

Last but not least, I want to say a big thank you to my family, Gabi, Günter, Michi, Nina and Luna. Thanks for enabling me to pursue my interests in doing my studies. Thanks for being my role models in so many aspects of life. Thanks for your unconditional love and support and for letting me become the person I am today.

Contents

1 Introduction and Motivation

In the last half of the 20^{th} and the beginning of the 21^{st} century, Moore's law quite accurately described the downscaling of silicon-based transistors in integrated circuits [1]. In the same time miniaturization took place in many other areas and our life would be unimaginable without powerful handheld electronic devices such as smartphones or laptops. Alongside the increasing computational power, a need for compact sensors emerged, allowing the devices to perceive and interact with their environment. An example is automatization in industry, where process monitoring became mandatory. This thesis will describe the development of a measurement scheme based on a sensor for chemical substances employing quantum cascade technology as a promising way towards monolithic integration for lab-on-a-chip applications [2].

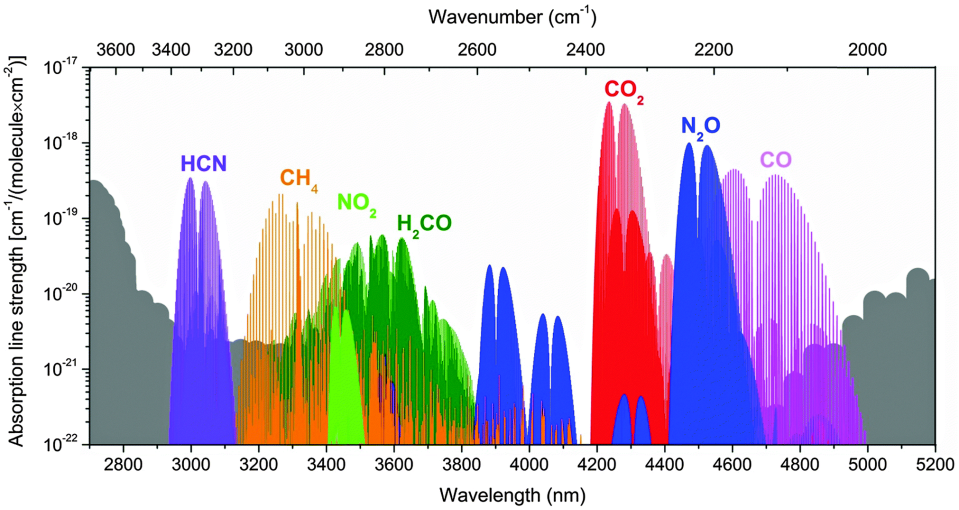

Figure 1.1: Absorption spectra of typical trace gases. The grey background indicates the absorption caused by water vapor. This figure was taken from [3], with data from [4].

Molecules show strong and very distinct absorption features in the mid-infrared (mid-IR) spectral region due to their fundamental rotational-vibrational energy states as depicted in Fig. 1.1. The sharp absorption lines only occur in the gas phase, in the liquid phase these peaks get significantly broadened

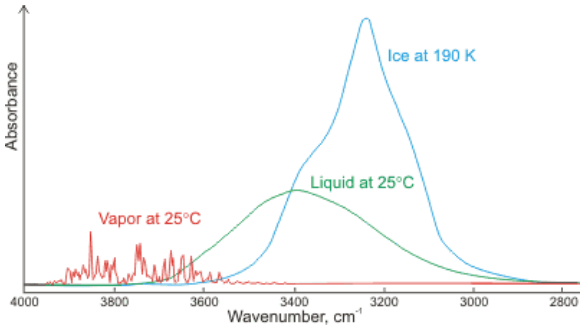

Figure 1.2: Absorption spectra of water in different phases: gaseous (red), liquid (green), solid (blue). This figure was taken from [5].

and partly overlap to wide spectral bands (Fig. 1.2). Since these spectra are unique for every molecule and even differ for varying structural conformation of the same molecule, the mid-IR, spanning from ~ 3 μm to 30 μm, is often referred to as "fingerprint region", making it quite appealing for sensing applications [6]. An additional benefit of IR radiation is its non-destructive interaction with matter, compared to ultra-violet (UV) light or even x-rays.

For a long time most of the available light sources in the mid-IR had major drawbacks concerning reliability, power output, coherence, stability and size, limiting IR optical spectroscopy to specialized laboratory equipment, until in 1994 the first quantum cascade laser (QCL) was shown by Faist et al. [7]. Within only a couple of years the first commercial QCL hit the market, while still being an active research topic today with more than 100 citations of the original article in 2019[†]. State of the art QCLs run in continuous wave (cw) operation at room temperature with Watt-level output power [8, 9] and dimensions on the millimeter-scale, opening up a platform for various applications.
One of the most important aspects about QCLs is the independence of the optical transition energy from the semiconductor bandgap and therefore the ability to tailor the device to work at almost any desired wavelength in the mid-IR and terahertz spectral region. The whole span from 2.6 μm [10] up to 1.2 THz [11] can be addressed, excluding the reststrahlen band. This property can be used to design a sensor directly targeting an absorption

[†]Web of Science: https://webofknowledge.com

feature of a molecule of interest.
Another interesting facet of this technology is that an unbiased laser functions as a detector, that, if designed properly, can efficiently detect the same frequency as the laser emits under biased condition [12]. This enables a relatively easy and cost efficient, monolithic sensor design as will be shown in the following chapters.
QCLs are applied in various fields. In environmental monitoring they are implemented to measure the atmospheric concentration of trace gases such as CO_2 [13], CH_4 [14, 15], etc. Sensors have been built for breath analysis in medical diagnostics to detect for instance NO [16] or acetone [17], as trace markers for certain illnesses. Applications are also found in industrial processes to in-situ monitor exhaust systems [18] or combustion processes [19], in security to detect explosives [20, 21] and even in radio astronomy as local oscillators [22].
Most of these examples measure the absorption of an analyte in the gaseous phase, which makes miniaturization challenging since large interaction volumes are advantageous to optimise the limit of detection, as gases have relatively high absorption lengths. The sensors in this thesis aim at the detection and analysis of liquid samples where molecules are much denser packed and therefore a respectively shorter path length is needed for comparable limits of detection. The dimensions of laser, detector and interaction region lie in the micrometer to millimeter range, making monolithic integration a promising concept for miniaturization and cost-efficient production.

The actual work performed continues where B. Schwarz (Monolithic integration of mid-infrared photonics) [23] and D. Ristanic (Optoelectronics Integration: On-Chip Infrared Sensors) [24] left off. Sensor chips that had been already processed were characterised and appropriate devices were chosen for experiments. Different approaches for a microfluidic cell implementing these sensors were tested. Absorption spectroscopy experiments were performed with the resulting setups, leading to a platform that can be used for diverse experiments in future works.
The thesis is structured as follows: it starts with a brief introduction on absorption spectroscopy. The subsequent chapters explain the physics of QCLs and QCDs before combining these building blocks to get to a working

sensor. Subsequently, device characterization, fluid cell development and finally absorption spectroscopy experiments are discussed.

2 Absorption Spectroscopy

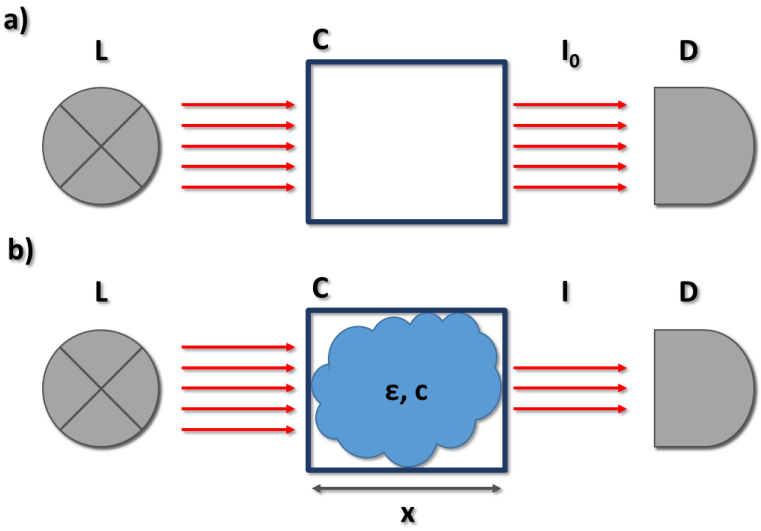

Figure 2.1: Absorption spectroscopy schematics: Light source L, Detector D, Incident light intensity I_0, Measurement Cell C, Transmitted intensity I, Molar attenuation coefficient ϵ, Molar substance concentration c, Optical path length x.
a) Empty-cell measurement for reference I_0, b) Measurement of transmitted I with filled cell and calculation of either ϵ or c.

The central equation in absorption spectroscopy is the Beer-Lambert law:

$$A(\lambda) = \epsilon(\lambda)cx \tag{2.1}$$

linking the absorbance A of a substance to the molar attenuation coefficient ϵ, the molar concentration of the attenuating substance c and the optical path length x. Both, the absorbance as well as the attenuation coefficient are dependent on the wavelength λ of the light travelling through the medium. The absorbance can also be defined as

$$A = \log_{10} \frac{I_0}{I} \tag{2.2}$$

with I_0, the incident light intensity and I, the transmitted light intensity.

These equations suggest a very simple experiment as illustrated in Fig. 2.1: The initial intensity of a light source is measured with a detector. In the next step a medium is brought in between the source and the detector, so the light can penetrate it for a known distance and the intensity at the detector is measured again. Knowing either the substance concentration or its molar absorption coefficient the respective other quantity can be calculated.
But this rather simple relation is only valid if the following criteria are fulfilled [25]:

- The incident light beam needs to be collimated and monochromatic.
- The substance needs to be homogeneously distributed across the beam cross section.
- Scattering within the substance has to be negligible.
- The substance concentration has to be low enough, so the interaction among the molecules is negligible.
- Scattering and reflection at the surface of the analyte has to be accounted for.

For polychromatic light sources their intensity spectrum and the wavelength dependent extinction coefficient have to be implemented into (2.1) and (2.2):

$$dI = I_0(\lambda)10^{-\epsilon(\lambda)cx}d\lambda \tag{2.3}$$

$$\text{with} \quad I_0(\lambda) = I_0 S(\lambda) \tag{2.4}$$

$$A = -log_{10}\left[\int_{-\infty}^{\infty} S(\lambda)10^{-\epsilon(\lambda)cx}d\lambda\right] \tag{2.5}$$

The normalized light source spectrum is given by $S(\lambda)$ dependent on the wavelength λ.
If an analyte consists of N different absorbing substances then their absorbances A_i simply add up:

$$A_{tot} = \sum_i^N A_i = x\sum_i^N \epsilon_i c_i \tag{2.6}$$

This formula indicates that in order to measure the concentration of a mixture of N substances, $N-1$ experiments with different known light sources have to be performed.
The theoretical evaluation of absorption spectroscopy experiments can be complicated due to uncertainties of the complex electro-optical system, therefore, commonly a sensor is calibrated and the calibration curve later on is used to interpret measurements.

3 Quantum Cascade Technology

The basic working principle of QCLs will be explained in this section, starting from single quantum wells building up a full device. Further on IR light detection using unbiased QCL structures will be addressed.

3.1 Quantum Cascade Laser

This chapter explains the basics of a QCL, starting from optical intersubband transitions to single quantum wells and finally a fully functioning laser. An even more detailed explanation to the topic can be found in [26].

One might assume that the functional principals of laser diodes and QCLs are somewhat similar, since both of them are electrically-pumped, semiconductor-based sources of coherent light, but actually they differ quite substantially. While in a laser diode the photon is generated when an electron in the conduction band recombines with a hole in the valence band (interband transition), in a QCL intersubband transitions take place. This means that the process of photon emission happens in either the valence band or the conduction band involving only one type of charge carrier, hole or electron, respectively. The name suggests the presence of sub-energy levels within the main band which has interesting consequences for light generation.

Figure 3.1 a) shows the optical interband transition in a potential well from the conduction band to the valence band with the energy difference E_{21}. Due to the opposite curvature of the two bands and the occupation of higher

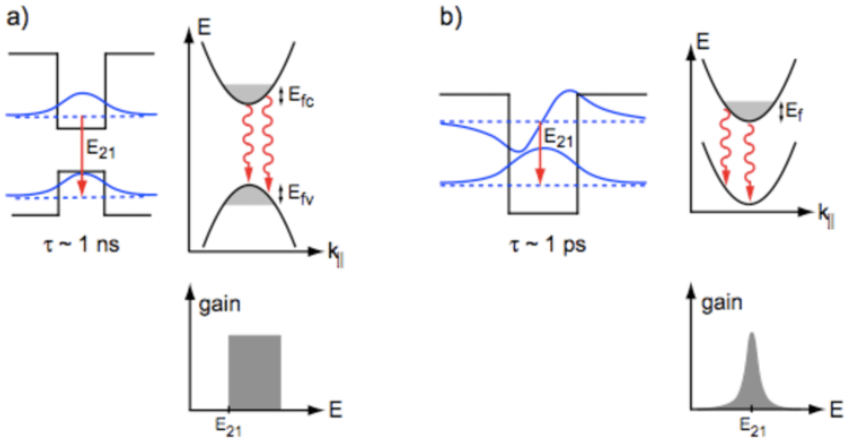

Figure 3.1: Band diagram, band structure and gain of a) interband transitions and b) intersubband transitions. This figure was taken from [27].

states, transitions with a higher energy difference than E_{21} can occur. This leads to a broad gain and respectively to a broad emission spectrum.
An optical intersubband transition is depicted in Fig. 3.1 b). Again the energy difference E_{21} separates the subbands, but in this case their curvature is the same (neglecting non-parabolicity). Therefore, independently of the occupied energy states, the photons end up having the same energy, resulting in a narrow gain and emission spectrum. In addition, intersubband transition photons are transverse-magnetically (TM) polarized due to the quantum mechanical selection rules.
Another unique property of a QCL is its cascading structure. The device consists of a periodical stack of regions where an optical transition is possible, therefore, one charge carrier can generate a photon for every step it takes in this cascade. This leads to a high differential quantum efficiency, enabling even devices with a small active region to operate at high output power [27].

The implementation of just one optical transition through a two-level system is not sufficient for laser operation. In order to reach population inversion at least a third energy level has to be implemented. The schematic working principle of a QCL is depicted in Fig. 3.2. Electrons get injected in the

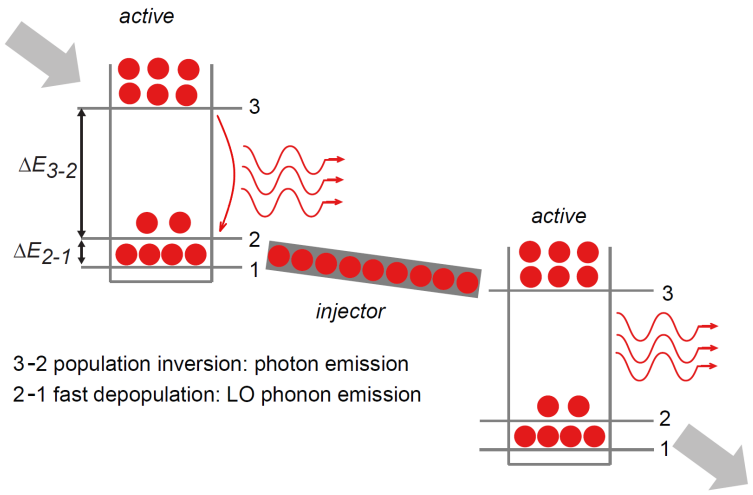

Figure 3.2: Schematic working principle of a QCL. This figure was taken from [24].

upper laser level (3), photons of energy ΔE_{3-2} are generated when electrons drop down to the lower laser level (2). The energy difference between level 2 and 1, ΔE_{2-1} typically equals the energy of a longitudinal optical (LO) phonon in the corresponding material system. Therefore, this transition is efficient and happens very fast. From level 1 the electrons are transferred into the upper laser level of the next cascading stage, usually by resonant tunnelling through a so-called injector region (multiple quantum wells).
The fast phonon-assisted depopulation of level 2 and injection into the upper laser level (3) create the population inversion and are responsible for the fast gain dynamics of QCLs, which lie in the order of picoseconds.

In order to understand the principle of the QCL a look at finite quantum wells, as shown in Fig. 3.3 a) and b), is useful. The energy for each eigenstate n can be calculated by

$$E_n = \frac{\hbar^2 k_n^2}{2m} \tag{3.1}$$

where k_n, the wave vector, is dependent on the width of the quantum well and the potential height. $\hbar$ denotes the reduced Planck constant and m the electron mass. The number of bound states is limited by their energy being smaller than the potential height. Consequently, a broader quantum well (a) possesses more bound states than a narrow one (b).

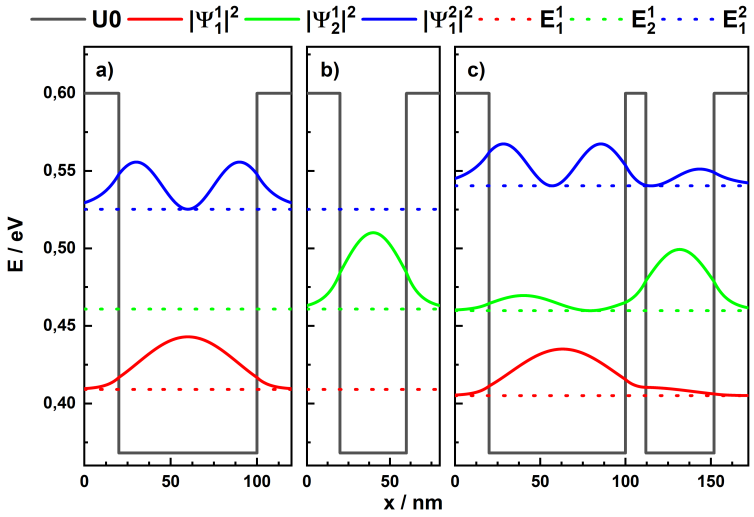

Figure 3.3: Electrons in a finite quantum well:
a) broad quantum well, b) narrow quantum well c) coupled quantum wells
$U0$... potential, $|\psi_w^n|^2$... probability density of state n in well w, E_w^n... energy of state n in well w.

Bringing the two wells into close proximity (Fig. 3.3 c) the wave functions of the separate wells spread out to the other well and couple to each other. This leads to a non-zero possibility for the electron to make a transition, calculated by the overlap integral.
A QCL consists of multiple quantum wells and barriers of varying widths, designed in a way as schematically shown in Fig. 3.2. An additional aspect important for the design is that during operation the QCL is biased, which tilts the bands and influences the wave functions. A typical QCL design is shown in Fig. 3.4. Commonly, the device consists of 20 to 50 periods, which in turn contain the active region and the injector. There is an overlap of the probability densities for the upper and lower laser levels for the optical transition and then on to the extractor state, typically separated by the energy of one LO phonon. Via scattering mechanisms and resonant tunnelling, the electron is injected into the upper laser level of the next stage.

The initial three well design was improved by reducing the spatial overlap of the upper and lower lasing level resulting in a diagonal transition. This increases the lifetime of the upper laser level and helps to build up a population inversion. There is a chance that electrons might be lost to the

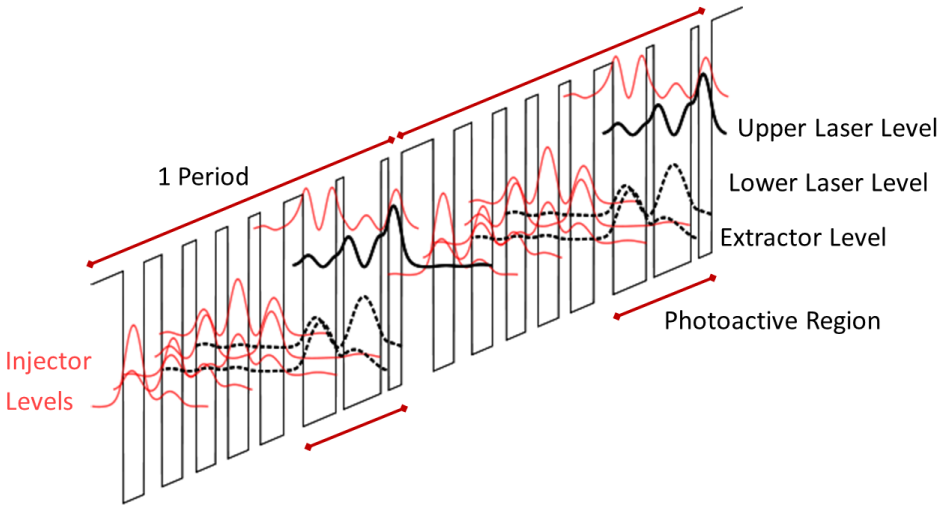

Figure 3.4: Band diagram of a three quantum well QCL with probability densities of the bound energy states. This figure was taken from [28].

continuum which can be counteracted by designing the injector as a Bragg reflector [29]. The next breakthrough that later on enabled cw operation at room temperature [30] was the so called two-phonon design. It features a fourth quantum well below level 1 from Fig. 3.2 to gain an additional energy level separated by a second LO phonon energy. This significantly reduces thermal back-filling from the extractor to the lower laser level even at higher temperatures.

A different approach implemented superlattices to create "minibands", similar to the energy bands in a crystal lattice [31]. Due to the long lifetime in the upper miniband and the fast scattering within a miniband, lasing can take place. This operation scheme was developed further to the "bound-to-continuum" design that combines the benefits of the original three quantum well design and the miniband approach [32]. The upper laser level is a discrete state, where electrons get injected via resonant tunnelling, while the lower level is a miniband, where electrons are quickly scattered to lower energy states. One advantage of this design is its broad gain caused by the transition between a single, discrete upper state to multiple closely-spaced states in the superlattice structure. The lasers used in this thesis are based on such a "bound-to-continuum" design.

In a real device these energy levels are realized by growing nm-thin layers of semiconductor materials with different band gap energies on top of each other, as shown in Fig. 3.5 d), referred to as a heterostructure. This forms the desired 1-D structure in the growth direction. The interfaces need to be abrupt and free from defects. Therefore, the different semiconductors in one QCL need to have matching crystal structures and similar lattice constants, while the growth of the structures is very challenging. Molecular beam epitaxy (MBE) [33, 34] and metalorganic vapor-phase epitaxy (MOVPE) [35, 36] are the favoured methods for that demanding task.

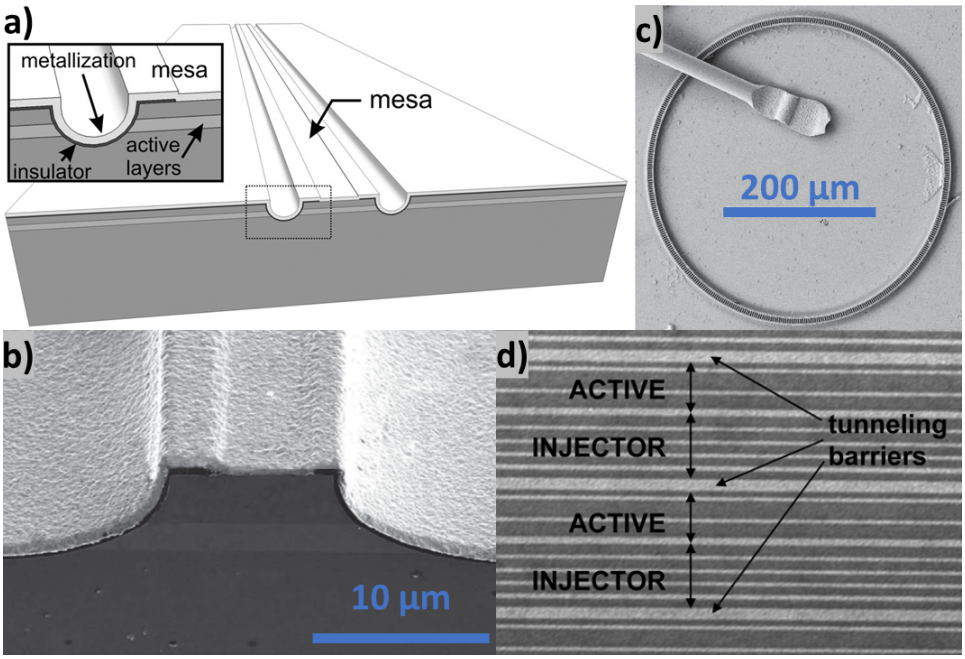

Figure 3.5: Laser device structures: a) Schematic of a typical QC ridge laser: two trenches define the laser geometry, an insulator layer enables the top device contact. This figure was taken from [37], b) SEM image of a QC ridge laser (active area in light grey). This figure was taken from [38], c) SEM image of a ring QCL with second order DFB grating. This figure was taken from [39], d) TEM image of a QCL active region. This figure was taken from [40].

The active region is typically embedded in a vertical (in growth direction) laser cavity. The light is outcoupled orthogonal to the growth direction (TM

polarization). The most commonly used cavities (or waveguides) of QCL devices are ridge and ring waveguides as shown in Fig. 3.5 a)-c). Usually the width of the devices is relatively narrow ($3 - 20$ μm), on the order of the emission wavelength, to feature only one lateral laser mode. The vertical confinement is achieved by the growth of additional, so-called cladding layers, on top and at the bottom of the active region.
In ridge type QCLs the back and front facets act as mirrors (reflectivity towards air ~ 30 %) to form a Fabry-Pérot (FP) cavity. Depending on the length of the cavity, a large number of laser modes will form. One of the facets might be covered with a high-reflection (HR) coating to maximize the power output at the other side. Ring type QCLs develop so called whispering gallery modes [41] and the light is coupled out vertically by second order distributed feedback (DFB) gratings.
The second reason to apply a DFB grating is to make the laser emit single mode radiation. By periodically modulating the refractive index of the cavity the modes inside get partially reflected and interfere. Only modes fulfilling the Bragg condition (3.2) interfere constructively:

$$m\frac{\lambda_{Bragg}}{2n_{eff}} = \Lambda_g \tag{3.2}$$

where m denotes the grating order, λ_{Bragg} is the free-space wavelength of light that satisfies the Bragg condition, n_{eff} the resulting effective refractive index and Λ_g the grating period.
Usually gratings are lithographically transferred and etched directly into the waveguide. The etching depth and the duty cycle of the grating determine the coupling strength. The order of the grating also determines the direction of light scattering. First order only couples in-plane, second order also scatters perpendicular to the initial mode direction.
As with many concepts in physics also QCLs can work in two directions: Light can be generated by a flowing current, but also a current may emerge upon light absorption, leading to detector operation.

3.2 Quantum Cascade Detector

In 2002 Hofstetter et al. published experiments using an unbiased QCL-like active material as a photodetector, somewhat similar to quantum well in-

frared photodetectors (QWIP) [42]. This concept works as a photovoltaic detector, meaning that a voltage builds up upon illumination and a photocurrent can flow. The working principle is depicted in Fig. 3.6: Absorption of a TM-polarized photon (black arrow) excites an electron (red dots) from the lower detector level to the upper one. In the upper level the electron resonantly tunnels to the extractor states, consisting of several levels separated by an LO phonon energy, and quickly gets injected into the lower detector level of the next stage. Due to the fast LO phonon scattering, near thermal equilibrium most of the electrons are located in the lower detector levels. As can be seen from the asymmetric band diagram, the electrons possess a preferential flow direction.

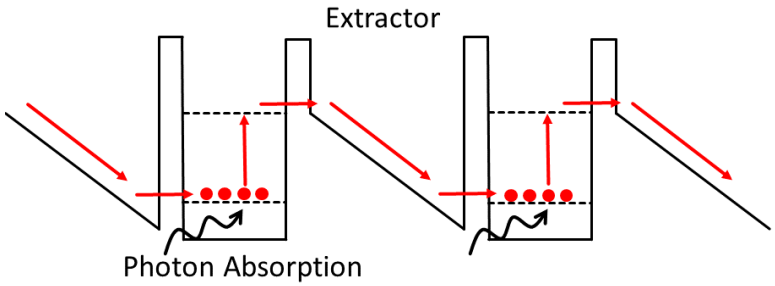

Figure 3.6: Schematic working principle of a QCD: A photon (black arrow) gets absorbed and excites an electron (red). The electron tunnels to the extractor and is injected into the next period. This figure was redrawn from [43].

The band diagram of a real detector working at 6 μm is depicted in Fig. 3.7, where in well A the active transition happens and wells B to F function as the extractor. This efficient extraction mechanism makes the QCD a very fast detector, that barely experiences saturation effects. Its responsivity is inversely proportional to the number of periods in the cascade and usually lower than that of a comparable QWIP. However, one of the main advantages of a QCD is its extremely low dark current even at high temperatures, due to unbiased operation, leading to better signal to noise ratio and the ability of long integration time measurements.

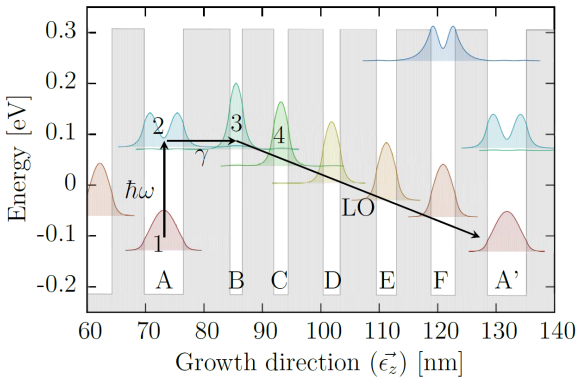

Figure 3.7: Band diagram and electron probability densities of a QCD for 6 μm wavelength: A photon $\hbar\omega$ gets absorbed in quantum well A and excites an electron from state 1 to state 2. Via resonant tunnelling γ it gets to state 3 in well B. LO phonon scattering leads to a fast extraction and injection into the next period, well A'. This figure was taken from [44].

This concludes the two essential modules (emitter and detector) of an absorption spectroscopic experiment. The next section introduces concepts essential for monolithic integration.

4 Monolithic Integration

In order to create a fully integrated on-chip sensor two aspects have to be considered: Firstly, the active region must be designed carefully to enable both laser and detector operation at the same wavelength. Secondly, the light must be efficiently coupled from the laser to the detector, so an additional waveguide has to be introduced.

4.1 Bi-Functional Active Material

This section briefly addresses the complex design issues of a so called bi-functional active region material - a material able to efficiently emit and detect light at the same wavelength. It is based on the publications [12] and [45] and explained in more detail in [23].

As shown in section 3.2, QCL active regions can be used for detection when unbiased. However, special care has to be taken in the design to compensate for a mismatch in the energy of emitted photons in lasing and absorbed photons in detecting operation. Fig. 4.1 shows the biased and unbiased case of a 4 well QCL to address this matter. The lasing transition (biased) takes place from the upper to the lower laser level. The detecting transition (unbiased), on the other hand, has its lower energy level originating from the previous injector, leading to a significant blue-shift of the wavelength compared to the lasing transition.

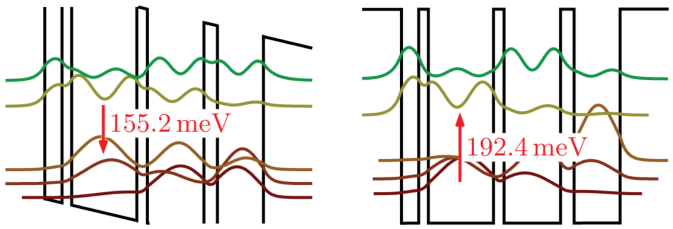

Figure 4.1: Comparison of the biased laser (left) and unbiased detector (right) operation of a common 4 well QCL. The difference of the emitted and absorbed photon energy is highlighted. This figure was taken from [12].

One approach to counteract the shift is to strongly couple the narrow well on the left in Fig. 4.1 to the transition well [12]. The width is designed so the energy level of its wave function matches the higher energy level of the active (broader) well, which leads to the degeneration of the energy. The lower level of these two is now used for the optical transition. This reduces the blue shift, but the effect is not strong enough to completely compensate it. Additionally, the coupling between the lower laser level and the extractor can be reduced, decreasing the mismatch so the spectral shift can be fully compensated. This comes, however, at the cost of a worse laser performance.

The breakthrough towards quantum cascade laser and detector (QCLD) devices that could compete with individual state-of-the-art lasers and detectors respectively was the horizontal-vertical extraction scheme [45, 46]. Fig. 4.2 illustrates the band diagram of an optimized device for laser and detector operation. Four regions can be discerned in laser operation: a

slightly diagonal optical transition takes place in the gain section (orange), which helps to reduce the wavelength mismatch. Next, the electrons are extracted almost horizontally through 2-3 quantum wells with thick barriers via scattering-assisted tunnelling (blue). These thick barriers enable a complete compensation of the wavelength mismatch. In the following vertical extractor (pink), strongly coupled wells with large energy differences prevent thermal backfilling and enable an efficient electron transport. The fourth section (green) is designed to effectively inject electrons to the next gain region in laser operation and extract electrons in detector operation. Two different energy levels are used respectively to optimize both modes.

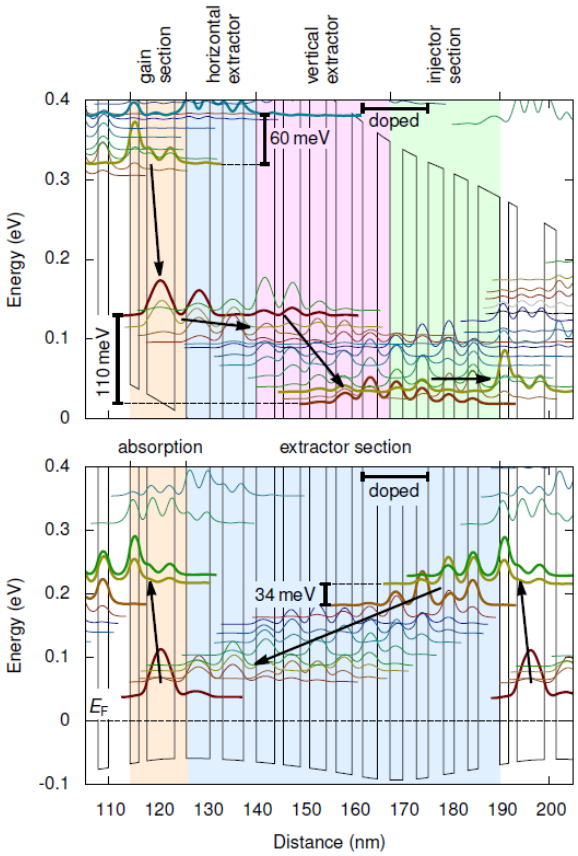

Figure 4.2: Simulated band diagrams for laser (top) and detector (bottom) operation of a QCLD active material, implementing the horizontal-vertical extraction scheme. The different regions are highlighted and the charge transport is indicated by black arrows. This figure was taken from [45].

This thesis was conducted using devices based on the discussed improvements. However, in 2017, a QCLD design was published able to operate in cw at room temperature with Watt-level output power [46].
After covering the theoretical background of the QCLD active region, the next section adds the last ingredient for the on-chip sensor and discusses how to efficiently couple the light of the laser to the detector.

4.2 Waveguiding

This chapter is based on the publications [23] and [47], where a more detailed explanation can be found.
Depending on the spectral region many different approaches for waveguiding have been realized. The field of plasmonics shows interesting concepts and is already well established in the visible and near-IR. In the last couple of years it spread to the mid-IR [48] and the sensors of this thesis exploit so called dielectric-loaded surface plasmon polaritons (DL-SPP) to efficiently couple the light from the laser to the detector, while maximizing the interaction volume with an adjacent analyte and keeping the additional processing costs at a minimum.
Surface plasmon polaritons are quasi-particles describing the strong coupling between the electromagnetic field and collective oscillations of charge densities at the interface of metals and dielectrics. They can be used to guide and localize electromagnetic waves. Dielectric-loading, the application of a thin dielectric strip, can be used for further mode confinement.

The necessity of waveguiding becomes clear with the simulations in Fig. 4.3. Without the implementation of a waveguide some of the laser light couples to the semiconductor substrate, but most of it is lost to free space (Fig. 4.3 a). If a gold surface is applied on the substrate in front of the laser, weakly bound SPPs are excited and the light couples to the metal-air interface (Fig. 4.3 b). This leads to a slightly increased propagation length. High lateral confinement can be achieved with the application of a thin and narrow silicon nitride (Si_3N_4, short SiN) layer on top of a gold surface (Fig. 4.3 c). The light couples to the metal-dielectric interface, which strongly binds the SPPs, leading to a drastically extended propagation length. Fig. 4.3 d) de-

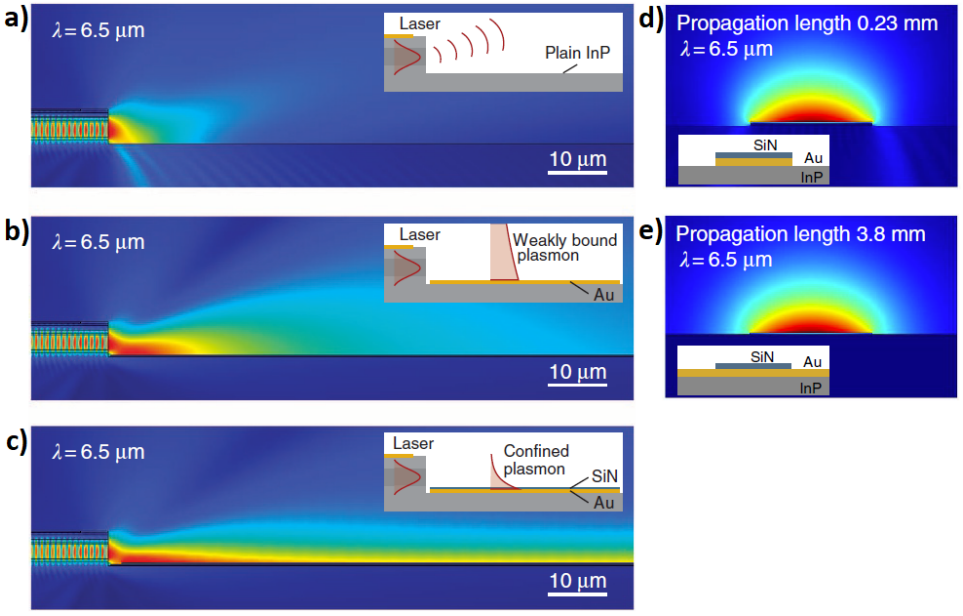

Figure 4.3: Simulation of electromagnetic wave propagation for different waveguide configurations: a) without waveguide: laser (left) emits most of the light to free space and partly to the substrate, b) a thin gold surface in front of the laser leads to the excitation of weakly coupled SPPs, c) a thin SiN strip on top of an unpatterned gold surface leads to a strong confinement of the laser mode to the interface and enhances the propagation length drastically, d) a thin SiN on gold strip leads to scattering losses at the metal edges, limiting the propagation length, e) the scattering losses can be avoided by a wider gold surface instead of a narrow strip. These figures were taken from [47].

picts the simulation of light propagation at the interface of a thin SiN-layer on a narrow gold strip, leading to scattering losses at its edges. These can be avoided by spreading the gold across a much larger area (Fig. 4.3 e), significantly prolonging the light propagation at the interface.
The TM-polarization of the light does not change when travelling through the waveguide, therefore, it can be directly coupled to a QCD. This leads to high coupling efficiencies from the laser to the detector even for longer waveguides.
Another important aspect of DL-SPP waveguides is that most of the mode (96 %) is located outside of the dielectric layer, leading to high interaction volumes with an adjacent analyte.

This concludes the building blocks of the QCLD on-chip sensors as a theoretical background for the following chapters.

5 Device Characterization

This section briefly introduces how a real sensor chip is grown and fabricated. Then, electrical and optical properties of the devices used for the experiments in this thesis are investigated.
The sensors were already completely fabricated in the in-house clean room facilities. The actual work of this thesis started with the mounting, wire bonding and characterization of the devices.

5.1 Sensor Growth and Fabrication

A brief overview of the steps necessary to yield a functioning sensor is depicted in Fig. 5.1: Starting with an InP wafer (1) the QCLD active region as well as cladding and contact layers were grown by molecular beam epitaxy. GaInAs was used for the quantum wells, AlInAs for the barriers and Si for n-type doping (2).
In the next step (3) the laser and detector ridges are processed by etching trenches into the epitaxially grown film (compare Fig. 3.5). Similarly, a DFB grating can be etched directly into the upper cladding layers of the

laser ridges. Both is done by reactive ion etching (RIE) [49], because of its anisotropic behaviour. SiN is used in step (4) to passivate the devices, so they can be electrically connected by extended contact pads from the top, without short-circuiting them. Gold is sputtered on to create these contact pads and the metal layer for the DL-SPP waveguides. Also, the dielectric SiN-strips are deposited in this step via plasma enhanced chemical vapour deposition (PECVD) [50].
Since many laser/detector pairs are processed simultaneously, in a last step the wafers are cleaved into smaller parts (usually 4-5 sensors per piece), which are subsequently mounted on a heat sink (e.g. Cu or Al) with In solder. The relatively soft solder metal compensates the different thermal expansion coefficients of sensor substrate and heat sink while still providing a good thermal conductivity. Finally, the devices are wire-bonded so they can be electrically contacted.

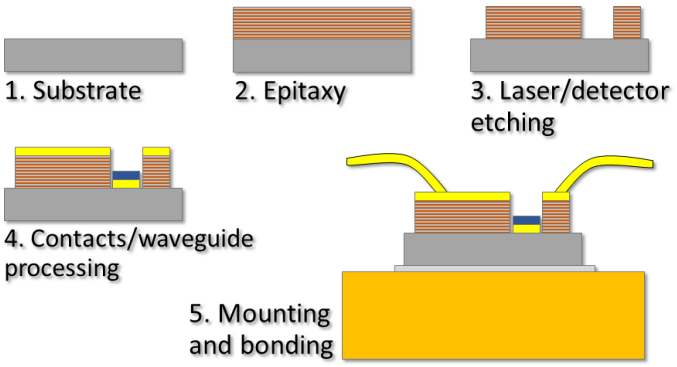

Figure 5.1: Growth and fabrication of a QCLD sensor, schematic overview: 1. A plain semiconductor wafer, 2. Epitaxial growth of the active region, cladding and contact layers, 3. Etching of the laser/detector ridges, 4. Processing of electrical contacts and waveguides, 5. Mounting of the substrate to a heat sink with indium and wire bonding of the electrical contacts.

To illustrate the working principle of the absorption spectroscopy experiments, Fig. 5.2 (left) depicts a rendered image of the sensor: Molecules between the laser and detector absorb the light and, therefore, lead to a decrease of the detector signal. On the right an SEM image of such a device is shown. The detector is a bit broader than the laser and the waveguide is

tapered to increase the coupling and as a consequence the detector signal. In the inset a zoomed-in image of the DFB grating in the laser ridge can be seen.

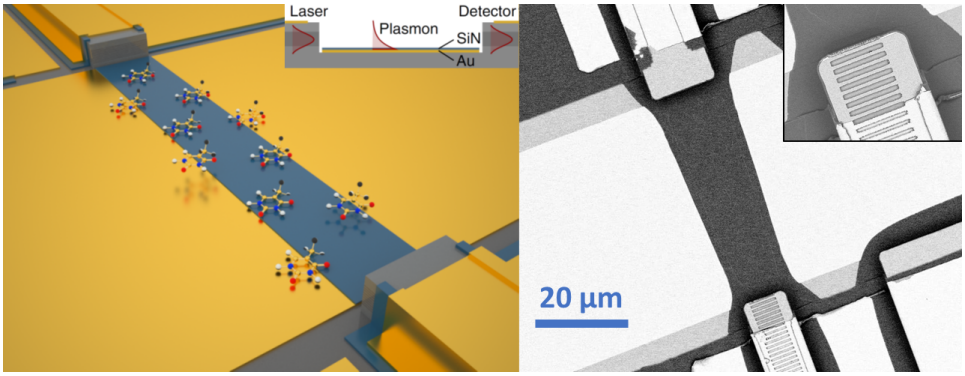

Figure 5.2: Monolithically integrated QCLD sensor: rendered image of laser and detector connected via a DL-SPP waveguide and absorbing molecules, with an inset of the cross section (left). This figure was taken from [45], SEM image of a fabricated device, the inset shows the DFB grating on top of the laser ridge (right). This figure was taken from [24].

The sensor chip used in this thesis consists of four laser-detector pairs as schematically shown in Fig. 5.3 (left) with its corresponding dimensions. The DFB gratings vary in a way that the lasers emit slightly different wavelengths around 6.1 μm ($\hat{=}$ 1640 cm^{-1}). The image on the right shows a mounted and wire-bonded sensor chip with six units of varying waveguide length.

5.2 Optoelectrical Characteristics

In all the experiments up to two QCLD sensors were used in parallel. They were pulsed in sequence using two AVTECH AVL-2-B pulse generators at 5 kHz repetition rate with a pulse duration of 100 ns ($\hat{=}$ 0.05% duty cycle) and a respective delay of 260 ns. This sequential operation was necessary to limit electrical crosstalk, since both sensors share the same electrical ground. 47 Ω resistors were added in series to get impedance matching to the driving circuit. The detector signals were recorded using a Teledyne

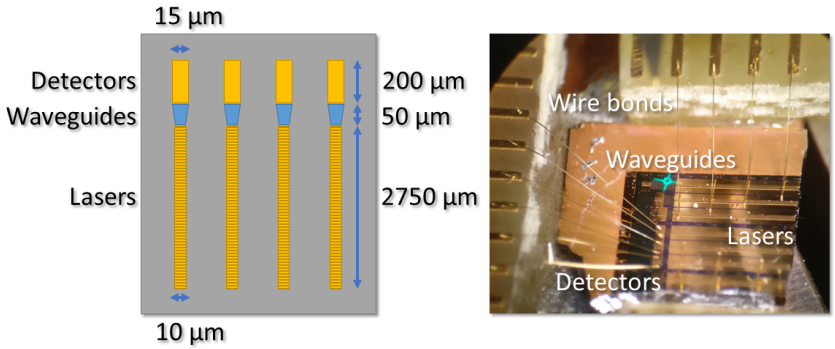

Figure 5.3: Monolithically integrated QCLD sensor: schematic of a semiconductor chip with four sensors (left), microscope image of a mounted and wire-bonded semiconductor chip with different waveguide lengths between lasers and detectors (right).

LeCroy HDO 4034 High-Definition Oscilloscope with 50 Ω termination. The area of the detected pulses was integrated by the oscilloscope to increase the signal-to-noise ratio (SNR), similarly to a boxcar averager, and transferred to the PC subsequently for post-processing. For the light intensity-current-voltage (LIV) measurements the oscilloscope was also used to measure the current through and the voltage directly at the lasers.
The resistance of a QCL and also its optical output power decrease strongly with increasing temperature. Therefore, on one hand the temperature had to be stabilized with a thermoelectric cooler driven by a Wavelength Electronics PTC 5 K-CH temperature controller, on the other hand a laser ridge can be used as a fast on-chip temperature sensor by continuously measuring its resistance with a Keithley System Source Meter (2636A/2612B).
The laser couples most of its light directly to the detector, so no absolute output power measurements could be performed, only the stray light can be detected externally.

The LIV of a laser ridge was measured using its on-chip detector and is depicted in Fig. 5.4. The laser voltage (black) looks typical for a mid-IR QCL. The laser threshold current density of 7.6 kA cm^{-2} can easily be seen in the red curve. However, at lower current densities a non-zero signal can be measured. This can be explained by electrical crosstalk: the laser and the detector are electrically connected via the substrate resistance. In order

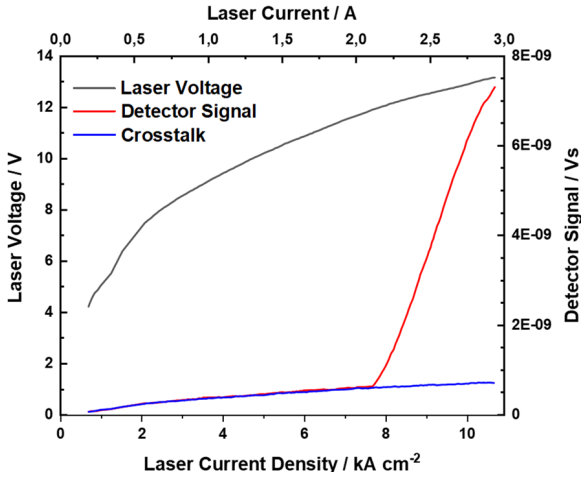

Figure 5.4: LIV measurement of the QCL: the laser voltage (black, left axis) follows a typical trend, the detector signal (red, right axis) shows that lasing starts at a current threshold of 7.6 kA cm^{-2}. The crosstalk signal (blue, right axis) was recorded at the detector by driving an adjacent laser.

to prove that theory, the detector signal was measured while an adjacent laser was operated and the result (blue) matches the recorded signal for the coupled laser below the lasing threshold. Above, it follows a similar trend and shows no jumps. Therefore, it is assumed that the crosstalk is mainly of electrical, not of optical nature. The signal can be used for crosstalk compensation calculations.

The laser emission spectra were recorded using stray light from the surface of the chip, collimated into a Bruker Vertex 70V Fourier transform infrared (FTIR) spectrometer. As shown in chapter 4.2, a large percentage of the laser light is coupled to the detector, making it difficult to obtain the spectra. A liquid nitrogen-cooled EG&G Judson mercury cadmium telluride (MCT) detector was connected to a Stanford Research Systems SR570 low-noise current amplifier, further enhanced with an EG&G 5210 lock-in amplifier to measure the faint spectral signal. The laser temperature and also the driving current influence the spectral behaviour. Therefore, a temperature range from 15 °C to 40 °C for various laser currents was investigated. Fig. 5.5 shows the normalized spectra of the two lasers most suited for the absorption spectroscopy experiments at three different temperatures. The intensity of the emitted light decreases with the temperature, but also the spectral

components vary quite substantially. The DFB gratings seem not to couple too well to the laser, since several peaks are visible. However, the two laser spectra differ sufficiently, qualifying them for absorption spectroscopy experiments.

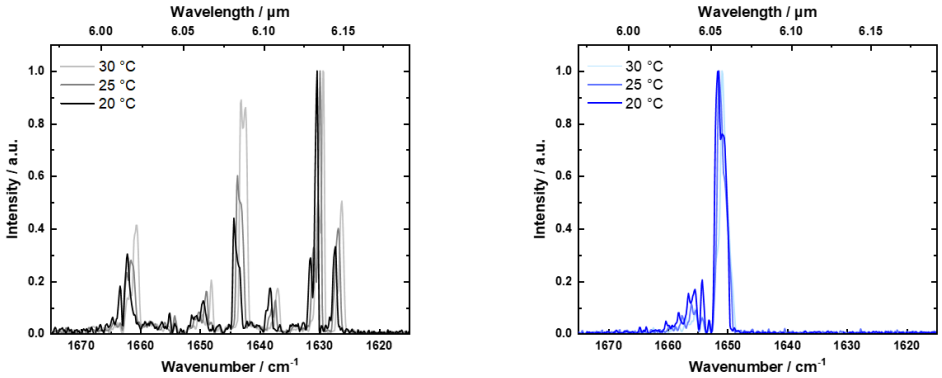

Figure 5.5: Spectra of QCLs on the sensor chip for varying temperatures: sensor 1 (left), sensor 2 (right).

After the characterization of appropriate devices an experimental scheme had to be developed and will be discussed in the next chapter.

6 μFluidic Cell

The design and processing of a microfluidic cell was one of the main parts of this thesis. It posed difficulties in various aspects, which were approached in several ways. The following list gives an overview of the design challenges:

- The fluid cell needs to be leak-proof and chemically stable. Depending on the experiments this can either mean acids and bases or organic solvents. It can also mean that the substances used are not degraded by the materials, e.g. biological cells by silver.

- Its volume should be as small as possible.

- The fluid connectors and the cell itself need to be mechanically stable.

- Both, the liquid has to reach the QCLD sensor chip, but also an electrical connection needs to be made to lasers and detectors. This means the chip has to be wire-bonded to a conductor path, leading out of the cell, so BNC-connectors can be soldered on to it.

- The QCLD chip needs to be connected to a heat sink. The in-house built Peltier coolers are all designed for 2.5 cm x 1.5 cm x 0.1 cm pure copper plates, which the lasers are usually soldered on with indium (cf. Fig. 5.1). Ideally, the fluid cell should be compatible to these, or even incorporate them.

The goal was to explore the capabilities of different approaches, while pursuing the more promising ones. In the beginning, two fundamentally different concepts were investigated:

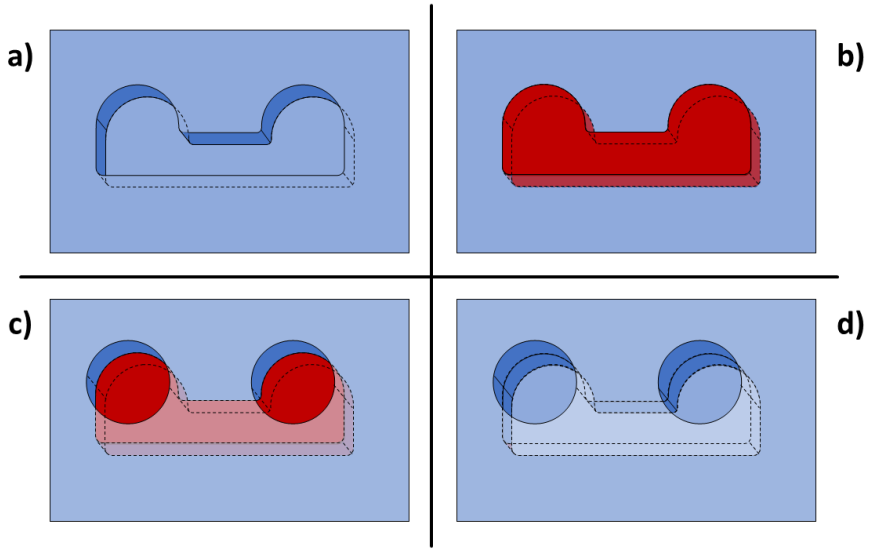

Figure 6.1: Schematic procedure of the microfluidic channel processing: a) a layer of SU-8 photoresist is spin-coated and the middle part gets removed by developing, b) the removed part is now filled with maP 1275 photoresist (red), c) a second layer of SU-8 is applied and circles are removed, d) the maP 1275 is dissolved in acetone, the underlying channel is opened.

The first one was inspired by a publication of Diehl et al. [51], who used lithography to create a microfluidic channel directly on top of a QCL chip

out of photoresist and polydimethylsiloxane (PDMS). In a first attempt a 7 μm high and 500 μm wide channel with openings for tubing were processed in SU-8 negative photoresist in three steps (see Fig. 6.1): a) a first layer of SU-8 was deposited on a GaAs substrate and lithographically patterned so the fluid channel and the tubing openings were removed (blue); b) a layer of maP 1275 positive photoresist was developed to cover the opening of the SU-8 layer (red); c) an additional SU-8 layer was deposited and only the tubing openings were patterned; d) the maP resist finally was removed with acetone, leaving the openings and the SU-8 covered channel. However, it appeared that the SU-8 slightly mixed with the priorly deposited maP, making it difficult to judge the quality of the channel. A microscopy image after the final step is displayed in Fig. 6.2. The red residuals of the maP 1275 photoresist can be seen clearly within the channel.

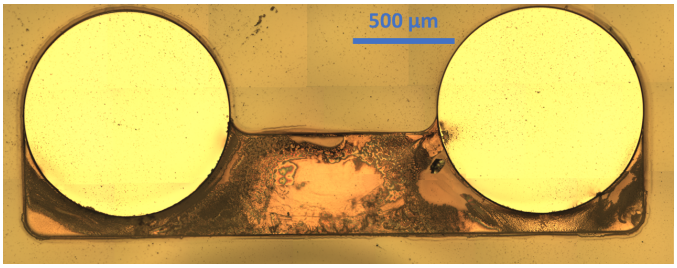

Figure 6.2: Microscope image of a lithographically processed microfluidic channel in SU-8 negative photoresist.

Another downside of this approach is, that the sensor chips are too small (2-4 mm width) to be processed with the clean room equipment. Also, it would be difficult to apply tubing that is mechanically robust. The devices would have to be soldered to a heat sink priorly, solving these problems. However, this would leave a step from sample to the heat sink, too high to perform precise lithography. Therefore, this approach was not investigated further. In future work the maP resist could be exchanged for one, that is not soluble in SU-8.

The second concept evolved around the aforementioned copper plate heat sinks and finally lead to successful experiments.

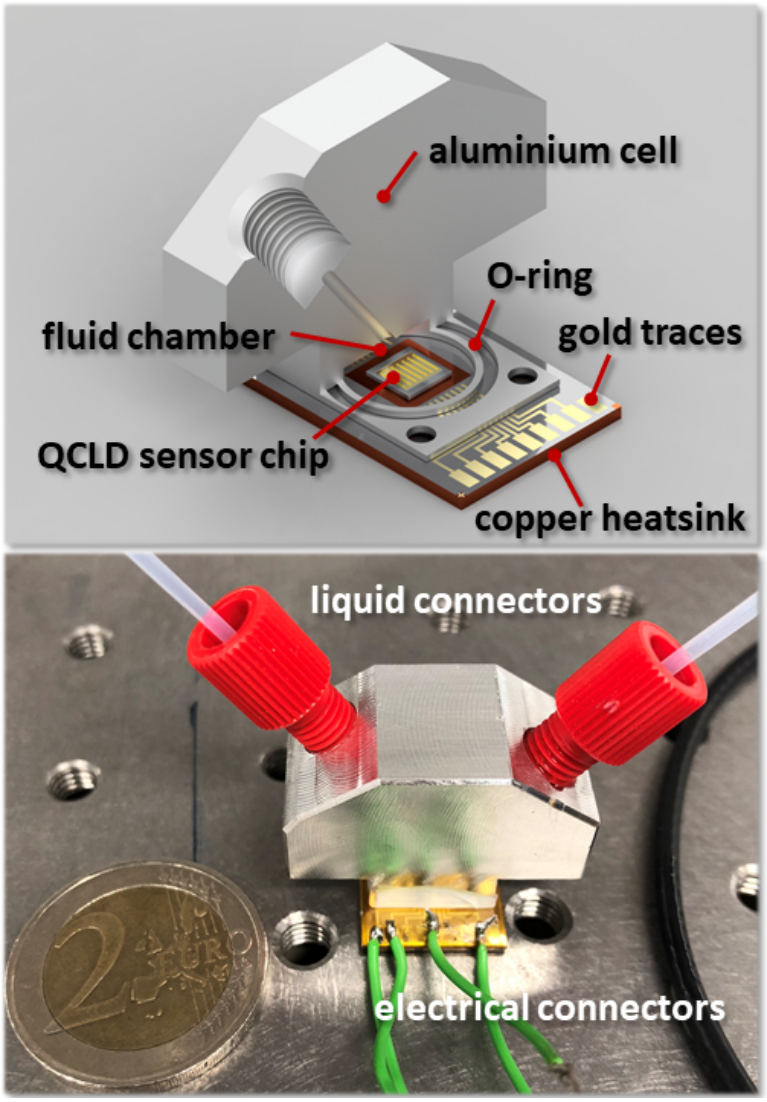

Figure 6.3: Rendered image of the microfluidic cell (top), final device with liquid and wire connectors (bottom).

The idea was to lithographically process an electric circuit board onto the copper plate and use a second bulk part forming the liquid cell, ultimately screwing both together and sealing the cell with an O-ring in between. A rendered image of the final design can be seen in Fig. 6.3 (top). The top part of the cell was manufactured in-house from aluminium, featuring standard flangeless liquid connectors and a cell volume of ~120 μL for the copper substrate and ~60 μL for an advanced aluminium substrate concept. The latter can be compared to the volume of a single drop of water only.
A chemically stable Teflon O-ring of 1 cm diameter in between the aluminium cell and the circuit board results in a leak-proof fluid cell.

The circuit board turned out to be more of a challenge and different designs were implemented. They are discussed in more detail in the following sections.

6.1 Copper Substrate

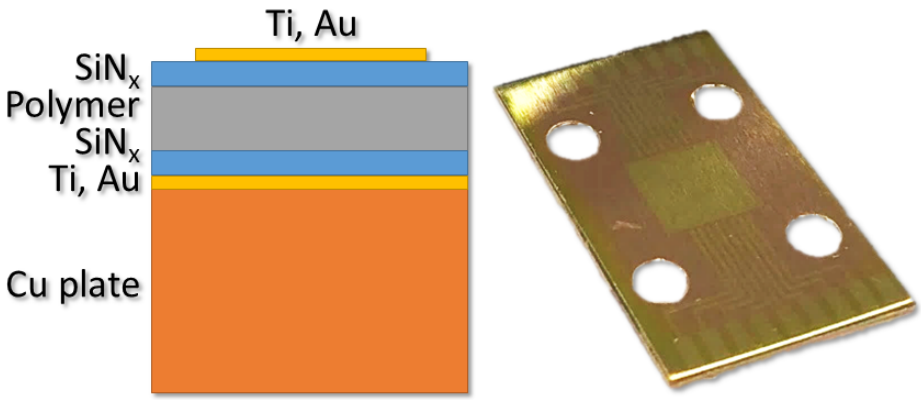

Figure 6.4: Copper circuit board: schematic cross section (left), fully processed (right).

When processing the circuit board on copper, two main issues emerged: firstly, using only a thin SiN insulation layer made it impossible to solder wires to the gold pads due to the fast heat transport. The copper substrate acted as a heat sink for the contact pads and cool the solder too quickly. Also, the thin layer was easily short-circuited by mechanical impact (e.g.

measuring the resistance with multimeter tips). Secondly, an SU-8 photoresist insulation layer led to delamination of the gold pads already under low stress from soldered contact wires and even wire-bonding ripped away parts of the gold traces. Therefore, a sandwich process was applied leading to the final recipe, which is depicted in Fig. 6.4:
Holes were drilled into the pure copper heat sink so the aluminium flow cell could be attached to it. It was mechanically polished and a thin layer of Ti (10 nm) and Au (200 nm) was deposited by sputtering. Subsequently, a 1 μm thick layer of SiN was deposited using PECVD. A layer of 8 μm SU-8 photoresist was applied by spin coating and the middle part was removed, i.e. developed after the outer area of the negative photoresist was exposed. Another 1 μm thick SiN layer was deposited on top and the SiN in the middle square of the plate was etched away by RIE, revealing the initial TiAu layer. Finally, the gold traces were deposited by patterning the desired structure with maN 1440 negative photoresist, sputtering Ti (10 nm) and Au (300 nm) all over the sample and removing the excess gold on top of the photoresist by dissolving the resist in acetone. Such a process is called a lift-off procedure.
The sensor chip could easily be soldered to the middle square and had a good thermal contact because all the insulating layers had been removed there. The wire bonding was still demanding and the parameters had to be optimized. Wires could be soldered to the gold pads due to the increased thermal insulation and the pads did not delaminate as easily as before. In order to increase the mechanical stability, thin and flexible wires were used and after soldering two-component epoxy resin was applied to further increase their resistance towards mechanical stress.
This design offers the best thermal conductivity and relatively good chemical stability since SiN is resistant to most substances, such as solvents. The downside is its extensively time-consuming processing, while it still suffers from partial delamination when e.g. ripping off the bond wires for exchanging the sensor chip.

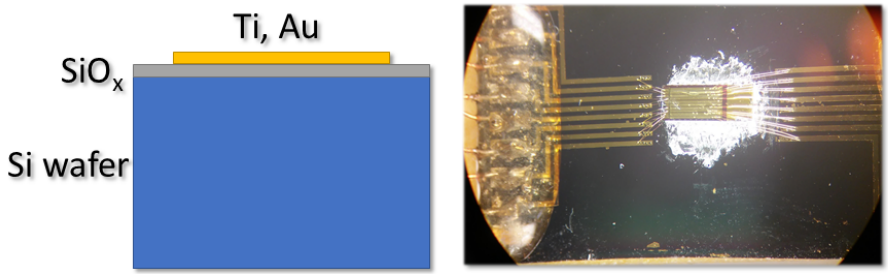

Figure 6.5: Silicon circuit board: schematic cross section (left), mounted, wire-bonded and soldered (right).

6.2 Silicon Substrate

Utilizing the findings of the copper circuit board, another design was developed, which started with a silicon wafer as a base, cleaved to the same size as the copper plates. A 1 μm thick silicon dioxide insulation layer was deposited on top of the pre-existing 50 nm dry SiO_2 by PECVD and, again, a Ti (10 nm) and Au (300 nm) lift-off procedure was used to create the electrical traces (see Fig. 6.5).
The sensor chip can be directly soldered onto the thin SiO_2 layer as a trade-off between processing time and thermal conductivity. The adhesion of the gold traces is similar, if not slightly better, compared to the copper design and the chemical stability is also sufficient for many applications. However, the difficulty lies in the drilling of the holes for attaching the fluid cell, without accidentally cleaving the substrate. This can be achieved by cautiously using dental diamond drills at high rotational speed while submerging the silicon substrate in a water bath.

6.3 Aluminium Substrate

The third solution was designed within the framework of this thesis, but ordered from an external manufacturer. It features an aluminium plate as a substrate, a polymer insulator layer with good thermal conduction and copper-gold traces that are partially protected by yet another polymer layer. In the middle a square was milled into the aluminium so that, after soldering, the sensor chip surface and the circuit board surface are roughly level.

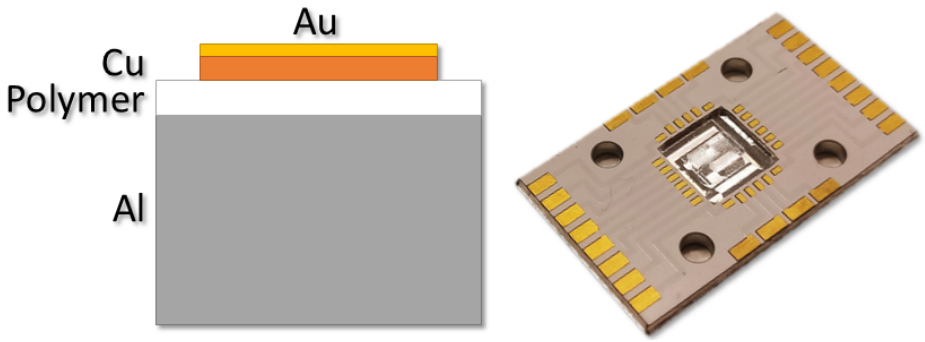

Figure 6.6: Aluminium circuit board: schematic cross section (left), photograph (right).

Compared to the other designs, this turned out to be the most practical one due to its good mechanical stability and wire bonding behaviour. Here, BNC-cables can be directly soldered to the gold contact pads without the need for thin and flexible wires in between. Furthermore, the 47 Ω resistor can also be directly soldered onto the contact pad to improve the radio frequency (RF) behaviour (cf. Fig 7.14).

For high power cw operation of QCLs a good cooling scheme and therefore the mounting on a good thermal conductor is essential. The devices in this thesis, however, are operated at a duty cycle of 0.05 %. Therefore, the thermal conductivity is less crucial. Tab. 6.1 lists the elements used for the circuit board and the laser substrate with their thermal conductivity.

Clearly, copper dominates the thermal behaviour, but also silicon has a rather high thermal conductivity compared to the InP-substrate, the devices are grown and processed onto. Additionally, the indium solder should be as thin as possible. The electrical insulators, on the other hand, are also thermally insulating and should be removed at the position the device is mounted to increase its performance.

In this design the whole sensor chip including the wire bonds is submerged in the analyte. The concern arose that the wire bonds might come off in a high liquid flux. Therefore, a liquid was applied directly with a syringe, rapidly emptying it through the fluid cell, to test rather extreme (mechan-

Table 6.1: List of Elements and their thermal conductivity [52–56].

Element	**Thermal conductivity / W m^{-1} K^{-1}**
Copper	401
Aluminium	220
Silicon	156
Indium	83.7
Indium Phosphide	68
SiO_2 (PECVD)	∼1.2
Si_3N_4 (PECVD)	∼0.5
SU-8	∼0.2

ical) conditions. Both, the copper and aluminium design were not affected by this procedure (cf. chapter 7.2).
Another aspect that has to be kept in mind is, that electrically-conductive liquids like acids and bases might short-circuit the laser. This was not investigated yet, but will be done in future work. If needed, the mounted sensor chip could be electrically insulated by applying either a layer of SiN or SiO_2, or sealing the electrical contacts with a photoresist, while implementing a microfluidic channel on the waveguides between lasers and detectors.

The performance difference of the three designs was not further investigated, as it can be assumed that their impact is rather small due to the low duty cycle operation. Furthermore, a temperature compensation scheme was developed later on, reducing the influence of the heat sink on the performance of the sensor even more. However, for optimization in future investigations this might become relevant.

With this, all the necessary components for experiments have been put together: a fully-operational QCLD liquid sensor chip has been mounted into a fluid cell and characterized next.

7 Absorption Spectroscopy Experiments

In this section various experiments that were performed with the microfluidic cell in the course of this thesis are presented. This includes the concentration determination, long-term behaviour and transient responses. Subsequently, the findings were used to do an in-situ concentration experiment. All of these experiments rely on a sensor calibration, while in the last subchapter a theoretical evaluation of the data will be addressed.
The conditions and lab equipment used to operate the sensor chip were identical to the ones stated in section 5.2, if not specified further.
In order to test the sensor a high and a low absorbing substance, namely H_2O and isopropyl alcohol (IPA), are mixed together in different ratios and pumped through the fluid cell.

7.1 Long-Term Stability

The first experiments were conducted on the copper mount with the 120 μl cell were aiming at investigating the long-term behaviour of the sensor. Therefore, it was cooled to 15 °C and driven by 100 ns pulses for over 3.5 hours at a sampling rate of $\sim$ 75 data points per second (Fig 7.1, black line). In order to find the best integration time the corresponding Allan deviation plot was calculated and depicted in Fig. 7.2. A detailed explanation on how to calculate the Allan deviation and interpret its results is given in [57]. The plot shows the Allan deviation in dependence of the number of averaged samples and features three main areas divided by the red lines. The most interesting one is in the middle. It corresponds to a region, where Gaussian noise dominates the signal, therefore, averaging improves the SNR. The right part corresponds to a region which is dominated by drift, which cannot be averaged out. It suggests that $\sim$ 20 000 samples should be averaged for optimum SNR. Even though the signal in Fig.7.1 still appears somewhat noisy, its standard deviation over the whole time is 0.001 A.U., which is equivalent to a concentration fluctuation of merely 0.05 $\%_{\mathrm{vol}}$.

No long-term drifts can be seen in the signal, which is a good indicator for a stable sensor operation.

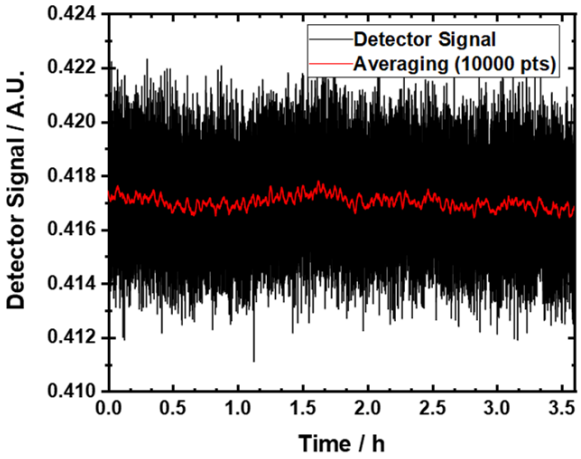

Figure 7.1: Long-term stability measurement of a typical QCLD sensor: time dependent signal (black), averaged signal (red).

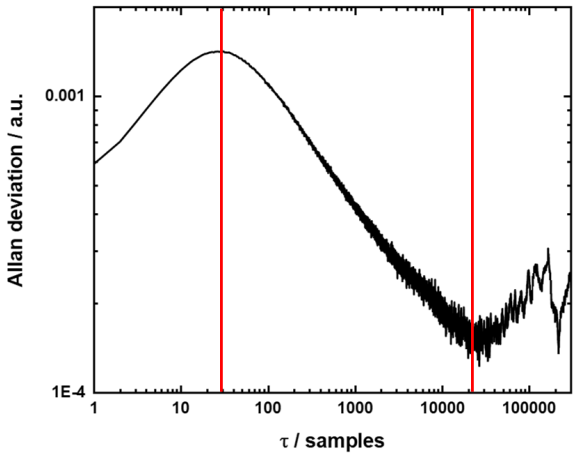

Figure 7.2: Allan deviation calculated from the long-term measurement of Fig. 7.1.

7.2 Transient Concentrations

Next, the copper-mount configuration with the 120 μl cell was tested for its transient response. Initially, the cell was filled with pure IPA, then a syringe was used to rapidly pump a solution of 80 % IPA and 20 % H_2O through the cell, followed by pure IPA again. The corresponding time dependent signal

is depicted in Fig. 7.3.

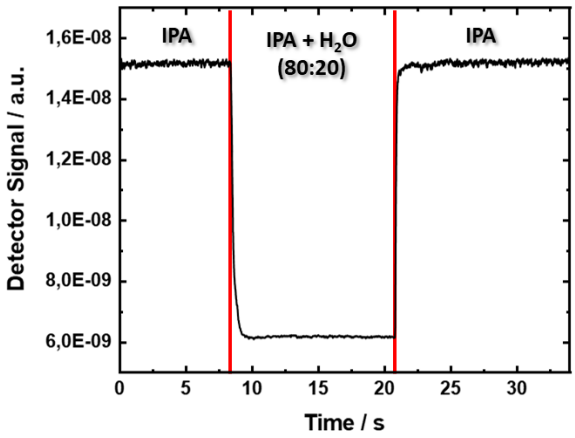

Figure 7.3: Transient concentration measurement with the QCLD sensor: pure IPA, IPA + H_2O, pure IPA applied to fluidic cell with a syringe successively.

The detector signal drops significantly (less than 50 % of the initial signal), but shows the same value before and after the experiment. The falling edge is shown in more detail in Fig. 7.4 and a double exponential fit is applied. The time constants show a very fast detector response, while the shorter one most likely corresponds to the flushing out of the preceding liquid, the longer one is caused by turbulence that occurs, when flushing the cell with a syringe and the mixing of the two liquids before getting flushed out completely. In any case the fluid cell geometry limits the response time of the sensor and not the laser or detector themselves. The time constants depend strongly on how fast the liquids are pumped through the cell, making a direct comparison difficult. Therefore, the cell volume was reduced significantly in the second design.

7.3 Water Concentration in Isopropyl Alcohol

For the following measurements the re-designed Al heatsink and PCB together with the 60 μl Al fluid cell were used, utilizing a new QCLD sensor chip. In Fig. 7.5 (left) the absorbance spectra of H_2O and IPA are depicted

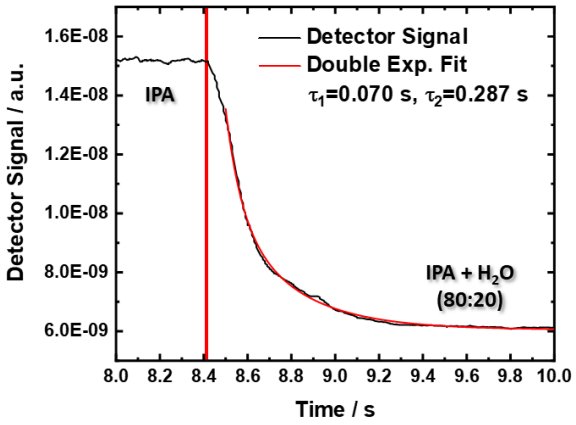

Figure 7.4: Transient concentration measurement with the QCLD sensor: pure IPA, IPA + H_2O applied to fluidic cell with a syringe, falling edge time signal (black) with a double exponential fit (red).

over the whole mid-IR spectral region. Also, the laser emission spectrum is plotted, but merely visible since it is a narrow line. The right image shows the highlighted section in more detail and reveals that for the laser light the IPA absorption is very low and almost constant (magenta), whereas the water absorption is extremely high (cyan). The absorbance was calculated for a 48 μm interaction length, which corresponds to the geometry of the 50 μm waveguide and 96 % of the optical mode being outside of the plasmonic waveguide, i.e. in the analyte, as discussed in section 4.2.

The QCLD sensor chip used in these experiments was processed with DFB gratings to enable single-mode operation. Slightly different gratings were used for each of the four otherwise identical lasers on the chip to address multiple wavelengths. However, the laser emission spectra in Fig. 7.5 show multiple peaks, leading to the conclusion, that the gratings do not couple well enough to the optical mode to sufficiently suppress all side-modes. Yet, the number of modes is significantly reduced, compared to a typical FP QCL. This leaves a lot of room for improvement, since single-mode lasers show a more stable operational behaviour. On the other hand, the spectra differ substantially, which allows to address different absorption features with each sensor unit, as intended.

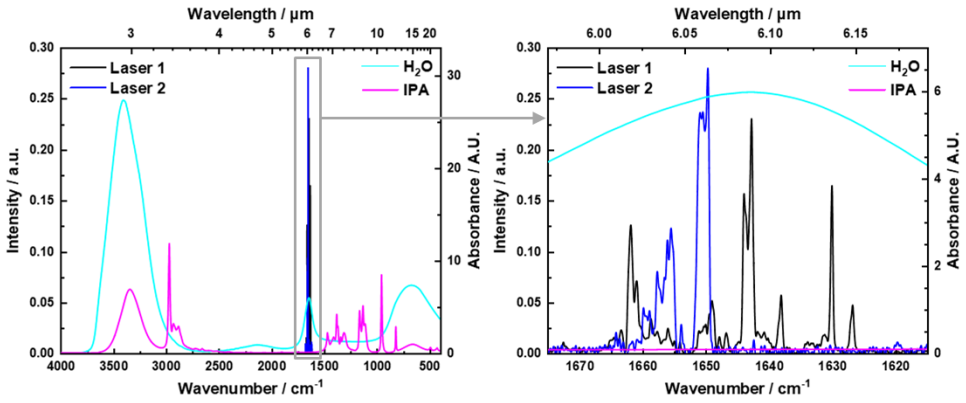

Figure 7.5: Emission spectrum of a QCLD sensor with two lasers working in parallel (black, blue) and absorbance spectrum of H_2O (cyan) [58] and IPA (magenta) [59] for a 48 μm interaction length: overview of the whole mid-IR spectral range (left) and zoom-in on the laser modes (right).

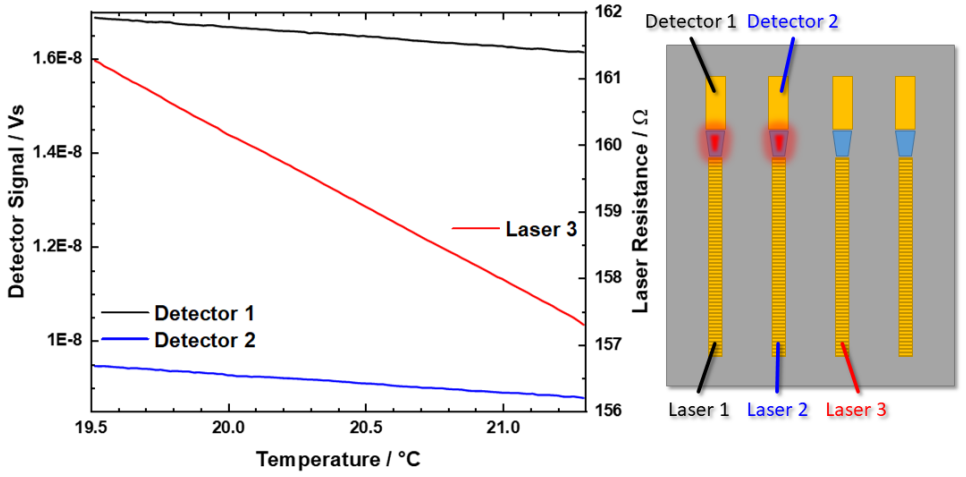

Figure 7.6: Temperature dependence of the QCLD sensor signals and the resistance of a laser ridge (left), schematic of a sensor chip with 4 laser/detector pairs (right): pairs 1 and 2 are used for absorption experiments, the resistance of laser 3 is used as a fast on-chip temperature sensor.

The schematic of the laser chip mounted within the fluid cell is depicted in Fig. 7.6 (right). Two lasers are driven in parallel and the light travels along the waveguides to their respective detector. On its path it interacts with the adjacent analyte and the intensity decreases. A third laser ridge is biased continuously to measure its resistance, which is inversely proportional to the temperature of the sensor chip. The fourth laser/detector pair is not used in the presented experiments. The pure IPA detector signal as well as the ridge resistance are recorded for many different temperatures, set with the Peltier cooler. It is crucial to wait for thermal equilibrium before taking the data points for every set temperature. Then, these curves can be linearly fitted and used to compensate temperature fluctuations in later experiments. The fit parameters are displayed in Tab. 7.1.

The intensity signal I measured at a detector varies not only over time t due to varying analyte concentration, but also with changing temperature T. The Beer-Lambert law (Eq. 2.2) can be used to compensate these fluctuations, if they are relatively small (single digit °C) and the intensity signal as a function of temperature is well represented by a linear fit. The detector signal can be approximated by a product of the temperature dependent intensity I_0 (the initial intensity in the Beer-Lambert law) and the concentration dependent transmission C (the exponential decay function in the Beer-Lambert law), which in the experiments mostly depends on the analyte, that varies with time (Eq. 7.1). With the temperature calibration curve from Fig. 7.6, the actual temperature can be calculated by measuring the resistance over time $R(t)$ and using the fit parameters from Tab. 7.1 with Eq. 7.2. The intensity term I_0 can now be written as a known intensity at a set temperature $\tilde{\mathrm{I}}_0$ altered by a temperature offset with the proportionality constant α_I (Eq. 7.3). To eliminate the temperature offset the equations are combined to Eq. 7.4, where, with the measured intensity $I_x(\mathrm{t})$ for sensor x, the time dependent resistance $R(t)$ and the fit parameters from Tab. 7.1, the temperature corrected intensity $\tilde{\mathrm{I}}_x(\mathrm{t})$ can be calculated.

$$I(T,t) = I_0(T) \cdot C(t) \tag{7.1}$$

$$T = \frac{R(t) - R_0}{\alpha_R} \tag{7.2}$$

$$I_0(T) = \tilde{I}_0 + \alpha_I (T - T_0) \tag{7.3}$$

$$\tilde{I}_x(t) = \frac{I_x(t)}{\left(\frac{R(t)-R_0}{\alpha_R} - T_0\right)\alpha_{I_x} + \tilde{I}_{0_x}} \tilde{I}_{0_x} \tag{7.4}$$

Table 7.1: Temperature compensation curves for the QCLD sensors, linear fit ($X = X_0 + \alpha_X T | X \in I_1, I_2, R$) of Fig.7.6: intensity signals of detector 1 and 2, resistance of laser 3, temperature T.

Device	$\alpha_{\mathbf{X}}$	$\mathbf{X_0}$
Detector 1 signal I_1	$-4.15 \cdot 10^{-10}$ $\frac{\text{Vs}}{^\circ\text{C}}$	$1.667 \cdot 10^{-8}$ Vs
Detector 2 signal I_2	$-3.82 \cdot 10^{-10}$ $\frac{\text{Vs}}{^\circ\text{C}}$	$9.26 \cdot 10^{-9}$ Vs
Laser 3 resistance R	-2.210 $\frac{\Omega}{^\circ\text{C}}$	204.36 Ω

In Fig. 7.6 the signal of detector 1 is almost twice the signal of detector 2, even though both lasers are operated at similar conditions. This might either be caused by a difference in laser performance, for instance by a too lossy DFB grating, or by different coupling efficiencies from the laser to the waveguide and further on to the detector. The latter might be caused by processing defects or even contaminations of the sample.

A piston-operated pipette was used to prepare 91 mixtures of IPA and H_2O with well defined concentrations. These were continuously pumped through the sensor and for each of the defined concentrations the detector signals were recorded and depicted in Fig. 7.7. Again, it was important to wait for thermal and concentration equilibrium before sampling.
The liquid transport was realised with an Ismatec Reglo ICC peristaltic pump[†], shown in Fig. 7.8. A fixed elastic plastic tube is squeezed by a small cylinder, that can rotate freely. This cylinder is moved along the tubing, pushing forward the liquid inside. In the used pump 8 cylinders are located

[†]https://www.ismatec.com/int_e/pumps/t_reglo/reglo.htm

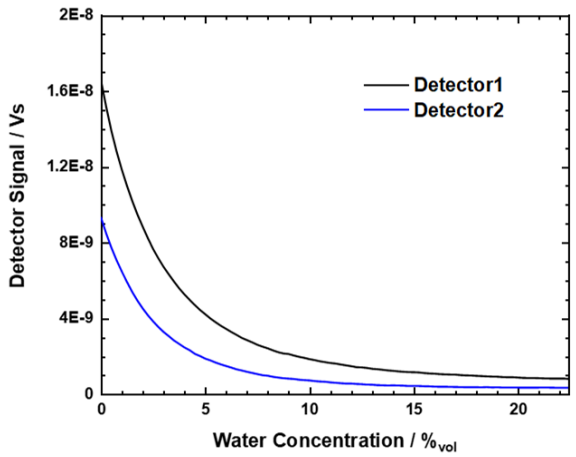

Figure 7.7: Calibration curve of the absorbance spectroscopy experiment: the QCLD sensor signals were recorded for an increasing H_2O-content in IPA.

in a circle on a disk. By rotating the disk at a certain speed, a desired pump rate can be achieved when the tubing diameter is known.

Figure 7.8: Ismatec Reglo ICC peristaltic pump for four independent liquid channels.

With the characterized sensors, the temperature compensation curve and the concentration calibration curve, finally, experiments were performed. The schematic is depicted in Fig. 7.9.

The sensor chip is located inside the Al cell on the Al heatsink and laser 1 and 2 are driven in parallel by individual pulse generators. A third laser is DC biased and its resistance is measured. The aluminium substrate fixed on a regulated Peltier cooler is set to 20 °C. The detector signals are recorded with an oscilloscope. A beaker with 50 ml IPA sits on a magnetic stirrer plate, a stir bar is inside the beaker. One tube leads from the beaker to the sensor fluid cell, over the peristaltic pump and back into the beaker. In the beginning of the measurement the pump stands still with IPA already in the fluid cell and at a certain point it is activated. This is done to check if the temperature compensation works properly, as will be explained later on. Another tube connects a beaker filled with pure de-ionized (DI) water over a second, individual channel of the peristaltic pump to the IPA beaker. This pump is only activated 15 min after the first one, so the stable operation can be guaranteed beforehand. With a flow rate of 1.5 ml/min water is then pumped to the IPA beaker, resulting in a drop of the detector signal over time. Due to the stirrer and a fast pumping of liquid through the sensor cell (15 ml/min) it is assumed that within the measurement circuit the water concentration is qualitatively the same. The theoretical water concentration can be calculated by

$$c_{H_2O_{\%_{vol}}} = \frac{1}{1 + \frac{V_{IPA}}{(t-t_0)\phi_{H_2O}}} \tag{7.5}$$

where V_{IPA} is the initial volume of IPA in the beaker, ϕ_{H_2O} the water pump rate, t the time and t_0 the time when the water pump started. This equation is valid after t_0, before, the theoretical concentration is zero.

In order to be able to measure fast concentration changes, while still conducting long-term experiments, multiple approaches were tested. The highest data rate for a continuous measurement was achieved with the following procedure. As mentioned before, the detector signals were integrated over the pulse length by the oscilloscope to increase the SNR. Thereby each pulse signal (or an average of multiple pulses) was converted into one single number. The oscilloscope then continuously generated a new time-dependent signal from these values with a buffer size of 1000 elements. This new waveform could be transferred to the computer, however, since no timing or

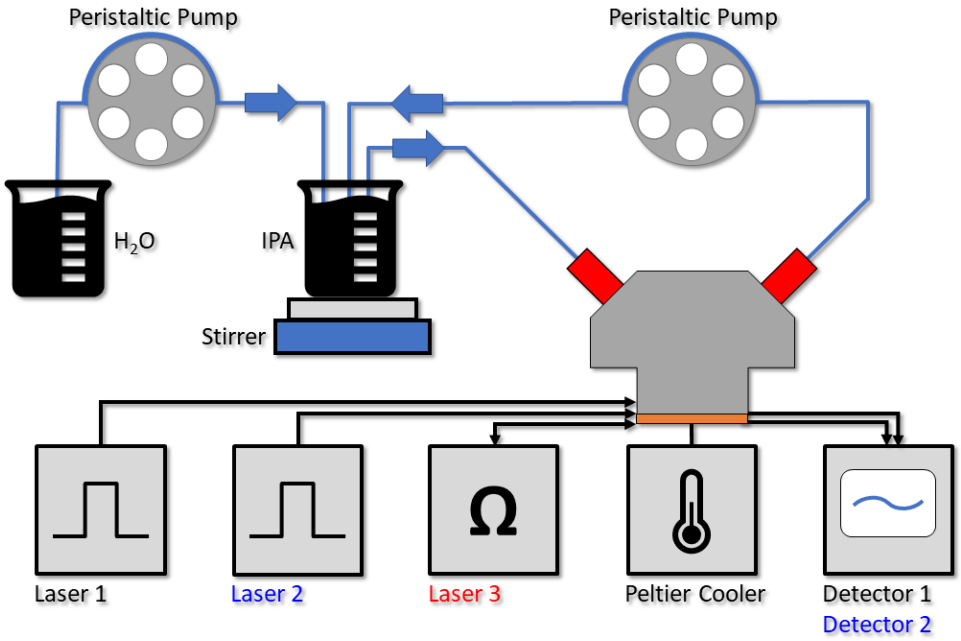

Figure 7.9: Schematic of the absorption spectroscopy experiment setup: pulse generators drive lasers 1 and 2, detectors 1 and 2 are read out with an oscilloscope. The resistance of laser 3 is measured for temperature compensation. The sensor is kept at 20 °C with a Peltier cooler and a temperature controller. Pure IPA is in a beaker and pumped through the cell constantly with a peristaltic pump. At a certain point a second peristaltic pump is activated to pump H_2O into the IPA beaker. A stirrer is used to rapidly mix the liquids.

triggering procedure was implemented in the system, the waveform had to be read out in a way, that two consecutive data sets overlapped in time. This overlap was used to stitch the waveforms together at the right position and generate the correct timestamps for each data point. This was implemented in a Python program and a fast algorithm was developed to find the overlap and merge the two datasets. It enables a continuous sampling rate of $\sim 170\ \mathrm{s}^{-1}$ for two channels simultaneously, where the individual data points are already an average of 5 pulses each. Furthermore, the application reads out the resistance of a third laser at a rate of 4 data points per second for the temperature compensation. It is also capable of operating the peristaltic pump.

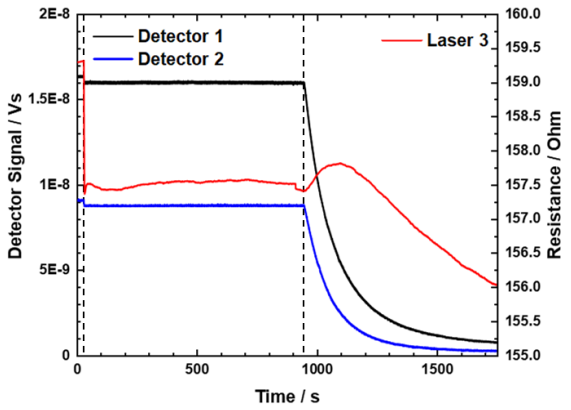

Figure 7.10: Absorption spectroscopy experiment: time dependence of the two detector signals (black, blue) and resistance of a laser ridge as a temperature reference (red) for increasing water concentration starting after 15 min.

An experiment according to Fig. 7.9 has been performed and the detector signals as well as the resistance of laser 3 are shown in Fig. 7.10. It can be divided into three subsections. In the first, pure IPA resides in the fluid cell. When the first channel of the peristaltic pump is activated to pump IPA from the beaker through the cell, the signal drops as well as the resistance. The cell is cooled to 20 °C, however the room is at a temperature of 22 °C, therefore the liquid within the unregulated beaker is warmer and heats up the cell and the sensor, resulting in this drop. Then, the signal is quite stable

for 15 min, until the second channel of the pump is activated to initiate the H_2O flow. With the increasing water concentration, the detector signals decay exponentially.

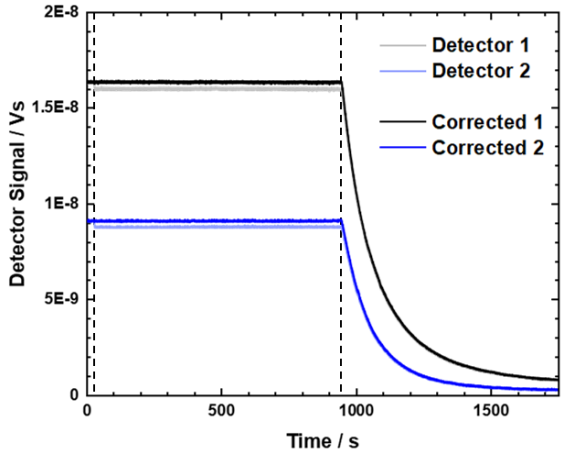

Figure 7.11: Absorption spectroscopy experiment: time dependence of the two detector signals (light black, blue) and temperature corrected (dark black, blue) for increasing water concentration starting after 15 min.

The resistance signal is used to calculate the temperature compensated detector signals with Eq. 7.4. Fig. 7.11 shows the measured detector signals in grey and light blue and the corrected signals in black and dark blue. The jump in the beginning vanished, which is a good indicator that the temperature compensation works properly.

Finally, the concentration calibration curve is applied to the temperature corrected intensity signal. By a simple mapping mechanism the y-axes of both, Fig. 7.7 and 7.11 are eliminated and the time dependent concentration signal is gained (Fig 7.12). The theoretical curve (green) is calculated using Eq. 7.5. For low concentrations both sensors are in good agreement with the theoretical value. At higher concentration the signals seem to become quite noisy. This is caused by the exponential behaviour of absorption. In this region there is almost no signal left, therefore, the noise increases steadily. This effect is more pronounced in sensor 2, which had a much lower signal to start with.

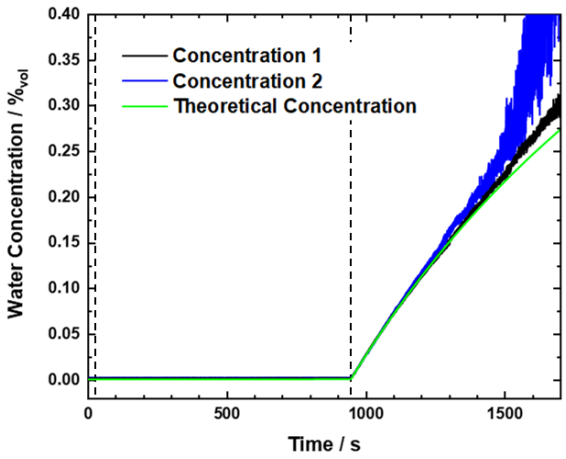

Figure 7.12: Absorption spectroscopy experiment: time dependence of the two temperature corrected detector signals, the concentration-calibration curve was used to convert the signals to water concentration in IPA (black, blue) for increasing water concentration starting after 15 min, theoretical curve (green).

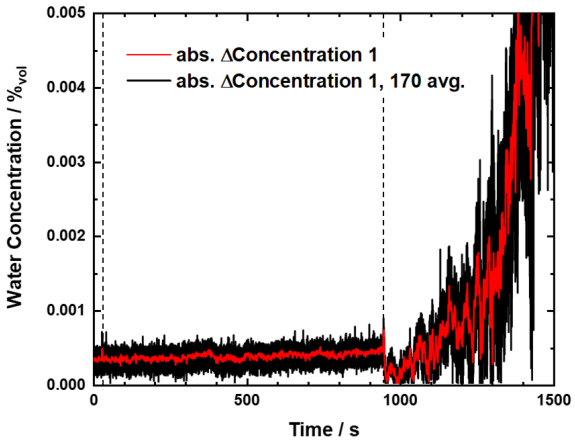

Figure 7.13: Absorption spectroscopy experiment: time dependence of the temperature corrected, calibrated detector 1 signal, the theoretical water concentration was subtracted and the absolute value was calculated for the normal time signal (black) and an averaged one (170 samples, red).

Fig. 7.13 enables a closer look at the deviations between theory and experiment. The theoretical signal was subtracted from the measured one of

detector 1 and the absolute value was formed (black). For the red signal an average over 170 samples was formed beforehand, leading to a sampling rate of $\sim$ 1 data point per second. In the beginning there is already an offset, which might be caused by a 370 ppm water contamination in the IPA. Although the supplier of the IPA guarantees a purity of 99.7 %, the residual 0.3 % might not be the source of the deviation, since the same IPA was used for the calibration curve already. One possible explanation might be, that water vapour from the air might have diffused into the IPA over time. When the pump is activated the deviation starts to increase, while also the noise is increasing, as mentioned before. This might originate from a slightly different pumping rate, but also evaporation of IPA might change the real concentration, which is not considered by the simple equation. After the measurement, the liquid was slightly white. Isopropyl alcohol and water might have slowly dissolved the peristaltic tubing, leading to an additional absorber that was not accounted for.

The standard deviation of the concentration signal for pure IPA is $8 \cdot 10^{-3}$ $\%_{\mathrm{vol}}$ and can already be reduced by a factor of 2 with the averaging of 170 samples, still leading to a data rate of 1 sample s^{-1}. This first experiment leaves a lot to investigate and optimize in future designs. One interesting finding is, that the temperature can be compensated quite sufficiently, enabling sensing without temperature regulation.

7.4 In-Situ Sensing

In-situ translates from Latin to "on site", in this context meaning that the measurement is performed directly at the spot, where a reaction is happening. Adapting the findings from the previous experiments and reusing the aluminium heatsink, a sensor was designed to be submerged completely in a beaker filled with an analyte for real-time measurement without a delay caused by liquid sampling before being analysed externally. Again, the experiment features two laser/detector pairs that can be operated in parallel and a third laser ridge functioning as a fast temperature sensor. The mounted QCLD chip can be seen in the middle of the sensor in Fig. 7.14.

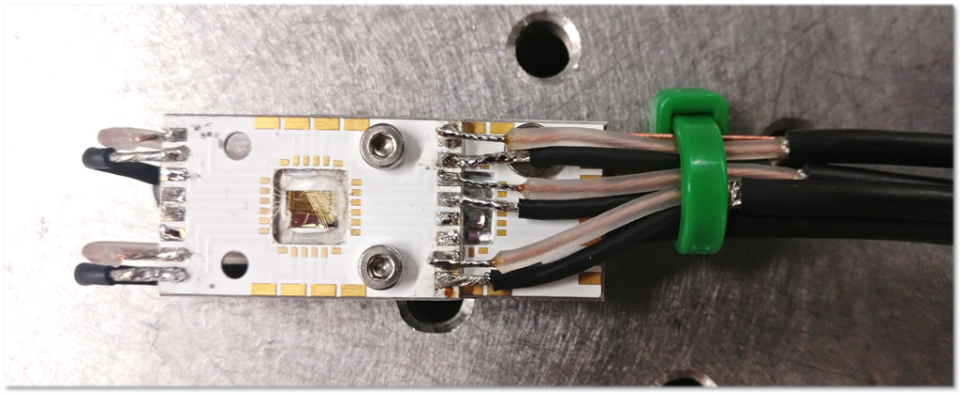

Figure 7.14: In-situ chemical sensor.

This approach has a slightly simpler measurement setup, compared to the one in the previous chapter. It is shown in Fig. 7.15. The electrical part is identical to the experiment with the aluminium fluid cell. The difference is, that now the sensor is directly submerged in the beaker, in which DI water and IPA are mixed. Again, a magnetic stir bar is used for that purpose, spinning directly beneath the sensor. It is activated after a short initial recording of the signals for a quick stability check. The initial IPA volume is 25 ml. The peristaltic pump is used to make water drop from a tube located above the beaker. Again, it will only be activated after a stabilization time of 7.5 min. A slow water flow rate of 200 μl/min has been chosen, to see a slower decay over a longer period of time. The whole measurement was set to take about 50 min.

The temperature compensation and concentration calibration have been performed beforehand. The raw time dependent signal of the experiment is depicted in Fig. 7.16. Again, three areas are immediately visible: a first very short one after which the stirrer is turned on and the intensity makes a small jump. This is followed by the stabilization and, ultimately, by the activation of the pump and the exponential decrease of intensity caused by light absorption in the added water.

The corrected and calibrated signals are displayed in Fig. 7.17. Compared to Fig. 7.16, the step at the beginning has vanished and also the falling

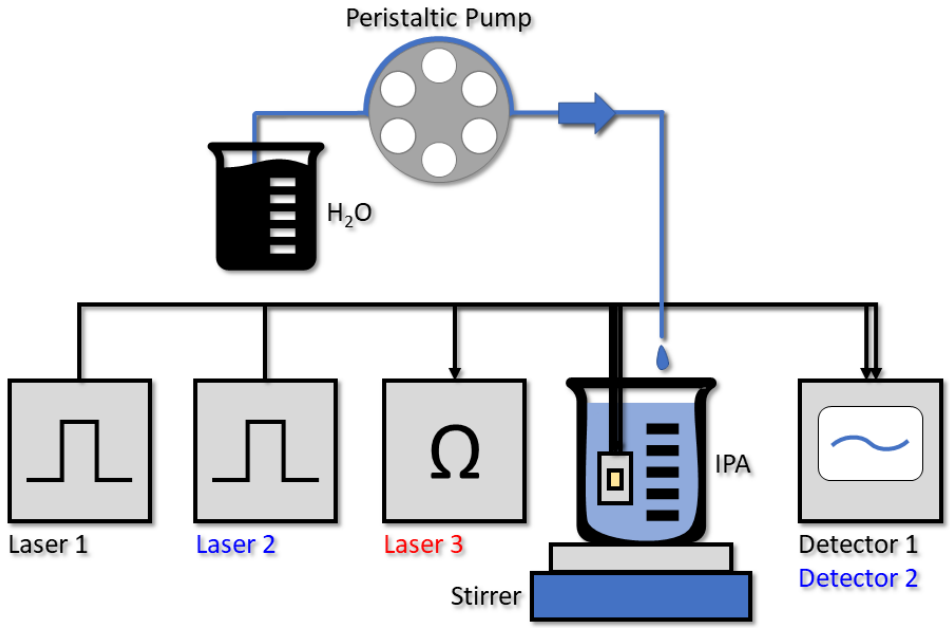

Figure 7.15: Schematic of the in-situ absorption spectroscopy experiment: pulse generators drive lasers 1 and 2, detectors 1 and 2 are read out with an oscilloscope. The resistance of laser 3 is measured for temperature fluctuation compensation. The sensor is submerged directly in a beaker filled with pure IPA. At a certain point the peristaltic pump is activated to drip water into the beaker. A stirrer is used to rapidly mix the liquids.

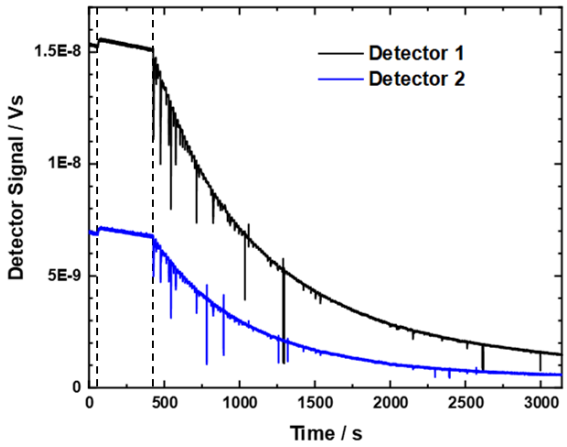

Figure 7.16: In-situ absorption spectroscopy experiment: time dependent signal of the two detectors (black, blue).

slope afterwards has been compensated with the temperature measurement. Both curves (black, blue) follow the theoretical one (green) quite well. The most prominent difference to the experiment with the fluid cell are spikes in the signal, implying very high and short peaks in water concentration. What is even more interesting is, that the peaks do not appear at the same magnitude for the two different sensors.
The explanation for this phenomenon is rather simple: when the water droplets hit the beaker, the swirl flushes the drops directly over the sensor before they completely mix with the rest of the liquid in the beaker. Depending on where the water is swept exactly the detectors measure different intensities, explaining the deviations of both corrected signals. In the long run, the steps caused by the droplets almost disappear and the envelope matches the theoretical curve.

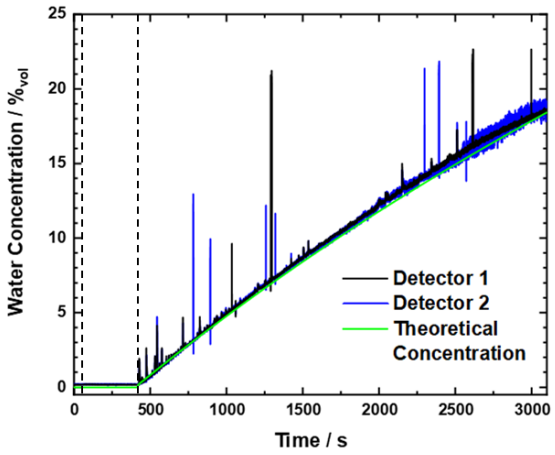

Figure 7.17: In-situ absorption spectroscopy experiment: time dependence of the two temperature corrected detector signals, the calibration curve was used to convert the signals to water concentration in IPA (black, blue), theoretical curve (green).

These peaks can actually be used to extract further information about the system. Fig. 7.18 shows the concentration signals caused by three consecutive droplets. The high peaks can easily be used to count the droplets. Furthermore, their positions in time can be used to calculate a droplet period Δt, in this case 15 s. The plateau of the step can be used to calculate the

volume of each droplet over the concentration difference $\Delta conc.$. The first droplet in Fig. 7.18 has 54 μl, which is in good agreement with an approximate 50 μl per drop. The flow rate then can be calculated to 216 μl min^{-1}, which also compares well to the set value of 200 μl min^{-1}.

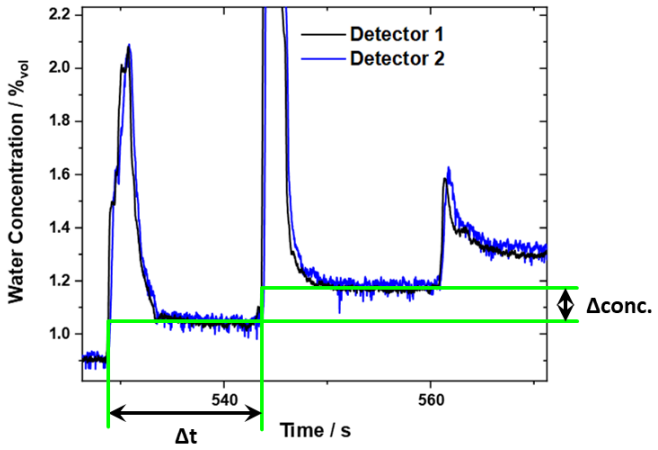

Figure 7.18: In-situ absorption spectroscopy experiment: concentration corresponding time signal of three consecutive droplets of water. The time difference Δt and the concentration difference $\Delta conc.$ lead to a droplet volume of 54 μl between two steps.

Additionally, the time constant for the mixing process can be extracted from the measurement, which varies around 1 s, depending on the exact droplet volume.

Here, the standard deviation for pure IPA is equal to $6 \cdot 10^{-3}$ $\%_{\text{vol}}$ and can be reduced to $5{\cdot}10^{-3}$ $\%_{\text{vol}}$ by averaging to get a sampling rate of 1 sample s^{-1}.

7.5 Theoretical Evaluation

As discussed in section 2, the evaluation of the measured signals can also be performed analytically instead of using a calibration curve, with some restrictions coming from the Beer-Lambert law. Starting from Eq. 2.1 the absorbance of water was calculated from the detector signals as follows:

$$A = \log_{10} \frac{I_0 - I_{cross}}{I(c) - I_{cross}} \tag{7.6}$$

whereas the crosstalk signal I_{cross} is measured for pure water, i.e. total absorption, and subtracted from the initial signal in pure IPA I_0, as a background matrix, and the intensities measured for the calibration curve at different water concentrations $I(c)$. These curves are depicted in Fig. 7.19 for both lasers (black, blue) for the fluid cell (left) and the in-situ experiment (right). Instead of the intensity in air, the pure IPA signal was used as the reference intensity to account for a difference between liquid and gaseous analytes, caused by different refractive indices at the interfaces.
The theoretical absorbance is calculated using Eq. 2.5 with the normalized laser spectra and the absorbance spectra (48 μm interaction length) of Fig. 7.5. The calculation was performed for all water concentrations used in the calibration curve and its result is plotted in Fig. 7.19 for both sensors (cyan, magenta).

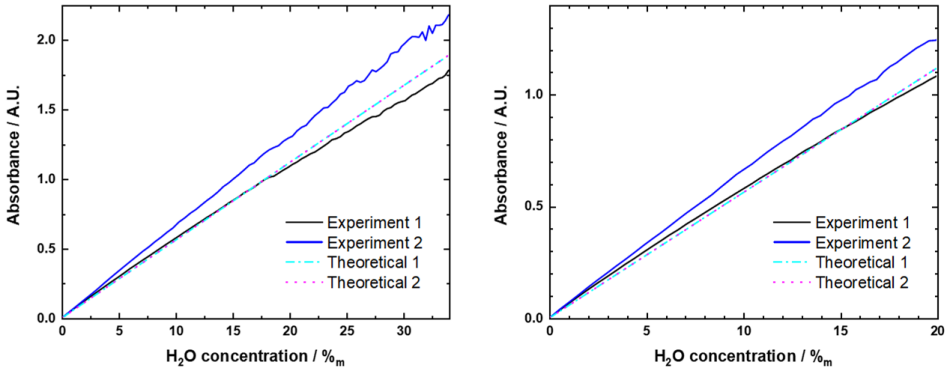

Figure 7.19: Theoretical absorbance computed with the absorption spectra of water and IPA for the emission laser spectra 1 and 2 (cyan, magenta), experimental absorbance calculated from the acquired data of the two sensors (black, blue) for the fluidic cell (left) and the in-situ sensor (right).

The experimental data for sensor 1 fits the theoretical curve quite well. At high concentrations the deviation becomes more pronounced. It might be caused by the limitations of the Beer-Lambert law, as discussed in section 2, since water and IPA are polar molecules that interact in a non-negligible

way. Furthermore, in the calculation IPA was used as the background matrix, which might not suffice for the high water content of the experiments. The data for sensor 2, however, is much higher than what is theoretically expected. One reason for this effect might be the fast and localized heating of the sensor chip due to the pulse of laser 1, preceding the pulse of laser 2 by merely 260 ns. This was not accounted for when the spectral measurements were performed. Fig. 5.5 shows that with increasing temperature the laser 2 peak shifts towards the center of water absorption in Fig. 7.5, while the side modes decline, both accounting for an overall higher absorbance.
Nevertheless, the calculated absorbances for two different calibration curves match each other quite well, substantiating the reliability of the sensor and being a good starting point for future experiments.

8 Conclusion and Outlook

A microfluidic cell was developed and implemented around a QCLD liquid sensor chip, operating between 6 and 6.15 μm wavelength. The long-term stability as well as the transient response of a prototype cell was investigated. Long-term drifts smaller than 0.001 A.U. were found for respective averaging of the signal, which compares to less than 0.05 $\%_{\mathrm{vol}}$ water concentration change. The transient response could be estimated with a double exponential fit revealing two time constants in the sub-second order of magnitude, indicating a fast mixing and liquid transport out of the cell. Moreover, the durability of the wire bonds was shown with this experiment.
A redesign and the implementation of a new sensor chip enabled experiments with an even lower volume of the fluidic cell, i.e. 60 μl, while being able to operate two independent sensors and a fast on-chip temperature sensor for improving the SNR simultaneously. In order to efficiently read out data over a long period a python script was programmed, leading to a sampling rate of 170 data points s^{-1} per sensor and 4 data points s^{-1} for the temperature signal. A calibration and a temperature compensation curve were recorded to extract the water concentration in IPA from experimental data. Using a peristaltic pump, water was added to IPA while continuously flushing the mixture through the cell. The processed data matches the theoretical con-

centration profile quite well.
The temperature compensation scheme allowed for the development of an in-situ liquid sensor. A similar experiment was performed, only now the sensor was submerged completely in an IPA-filled beaker, while water was dripping into the beaker at a well-defined and constant rate. Again, the calculated concentration ramp fits to the measured data nicely.
Furthermore, single droplets could be counted and their volume calculated, both being in good agreement with the set flow rate and the theoretical volume of a water drop. Additionally, the time constant of the mixing process of single drops could be estimated to ~ 1 s.

The presented work offers basic concepts for two types of liquid sensors, which can be further developed and implemented in various ways. The proof-of-principle experiment with water in IPA can be used to also detect other substances of chemical interest. The wavelengths of the lasers were chosen to target the absorption features of proteins, more precisely, the absorption originated in their secondary structure. Depending on whether a protein is curled up in a helical shape (α-helix) or planar (β-sheet) their absorption varies slightly. Fig. 8.1 (left) depicts this shift for β-lactoglobulin (BLG). A reaction from one to the other structure can be caused by temperature variations, but also certain pH-values favour one shape or the other. In the case for BLG an increasing pH-value leads to a transition from β-sheet to a disordered secondary structure, whereas the shift can be in principle recorded with the presented sensor. The difficulty is to overcome the high absorption of water, which in this case can be easily accomplished by making the measurement in heavy water (D_2O), which has a shifted absorption peak and does not interfere with this measurement. Another challenge in the case of acidic and basic environments is the electrical conductivity of the liquid. The sensor has to be electrically insulated, which can be realised by coating the sensor with a photoresist, lithographically clearing the area of the plasmonic waveguide. Alternatively, the sample could be coated with a thin layer of silicon oxide or nitride within a PECVD reactor.

Another example is alcohol induced denaturation of α-chymotrypsin. The formation of the β-sheet secondary structure can be observed by the emer-

gence of two new absorption features, while the main peak decreases, as can be seen in Fig. 8.1 (right).

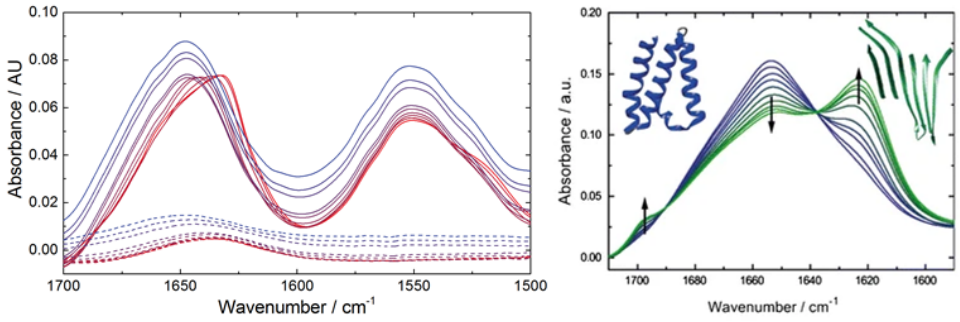

Figure 8.1: Absorbance spectra of proteins: an increasing pH-value shifts the peaks of β-lactoglobulin from the red to the blue curve (left). This figure was taken from [60], α-chymotrypsin is denaturated by alcohol to form β-sheets: transition from α-helix (blue) to β-sheet (green, right). This figure was taken from [61].

The devices allow various experiments that can be performed with the existing concepts, while still offering a lot of room for improvement. The fabrication of the microfluidic cell as discussed in the beginning of chapter 6 can be further developed by following the recipe of [51] to process a thin channel at the waveguide region. This would enable the cell to work with fractions of the current volume and also insulate the electrical contacts.
Similarly, a fluidic channel can be processed on a silicon wafer. The sensor chip then can be wafer-bonded directly onto it.
The diversity of QC technology can be exploited to detect molecules by tailoring the wavelengths of the devices specifically. For biological sensing the spectral region below 6 μm is very attractive due to the low water absorption, as shown in Fig. 7.5. Furthermore, depending on the experiment, the waveguide length can be designed appropriately with the findings of the initial experiments presented in this work. For high sensitivity of low concentrations, longer waveguides might be preferable, whereas highly absorbing species in vast amounts can be detected implementing shorter waveguides. Another angle for improvement is the electrical read-out of the detector signal. A current and/or lock-in amplifier can be used to further enhance the

signal and even a PCB can be designed so impedance converters can be put directly next to the detector.
DFB gratings can further improve the stability of the lasers if designed properly. A single mode laser is more stable to temperature and current fluctuations. This also influences the applicability of temperature fluctuation compensation in a positive manner.

References

[1] G. E. Moore, "Cramming more components onto integrated circuits. In: Electronics", *Electronics*, vol. 38, no. 8, 1965.

[2] L. R. Volpatti and A. K. Yetisen, *Commercialization of microfluidic devices*, 2014. DOI: 10.1016/j.tibtech.2014.04.010.

[3] M. Vainio and L. Halonen, "Mid-infrared optical parametric oscillators and frequency combs for molecular spectroscopy", *Physical Chemistry Chemical Physics*, vol. 18, no. 6, pp. 4266–4294, 2016. DOI: 10.1039/c5cp07052j.

[4] L. Rothman, I. Gordon, Y. Babikov, A. Barbe, D. Chris Benner, P. Bernath, M. Birk, L. Bizzocchi, V. Boudon, L. Brown, A. Campargue, K. Chance, E. Cohen, L. Coudert, V. Devi, B. Drouin, A. Fayt, J.-M. Flaud, R. Gamache, J. Harrison, J.-M. Hartmann, C. Hill, J. Hodges, D. Jacquemart, A. Jolly, J. Lamouroux, R. Le Roy, G. Li, D. Long, O. Lyulin, C. Mackie, S. Massie, S. Mikhailenko, H. Müller, O. Naumenko, A. Nikitin, J. Orphal, V. Perevalov, A. Perrin, E. Polovtseva, C. Richard, M. Smith, E. Starikova, K. Sung, S. Tashkun, J. Tennyson, G. Toon, V. Tyuterev, and G. Wagner, "The HITRAN2012 molecular spectroscopic database", *Journal of Quantitative Spectroscopy and Radiative Transfer*, vol. 130, pp. 4–50, 2013. DOI: 10.1016/J.JQSRT.2013.07.002.

[5] G. E. Ewing, M. Foster, W. Cantrell, and V. Sadtchenko, "Thin Film Water on Insulator Surfaces", in *Water in Confining Geometries*, V. Buch and J. P. Devlin, Eds., Berlin, Heidelberg: Springer Berlin Heidelberg, 2003, pp. 179–211. DOI: 10.1007/978-3-662-05231-0_9.

[6] Marwa El-Azazy, *Infrared Spectroscopy: Principles, Advances, and Applications*. IntechOpen, 2019. DOI: DOI:10.5772/intechopen.73071.

[7] J. Faist, F. Capasso, D. L. Sivco, C. Sirtori, A. L. Hutchinson, and A. Y. Cho, "Quantum Cascade Laser", *Science*, vol. 264, no. 5158, 553 LP –556, 1994. DOI: 10.1126/science.264.5158.553.

[8] D. Botez, J. D. Kirch, C. Boyle, K. M. Oresick, C. Sigler, H. Kim, B. B. Knipfer, J. H. Ryu, D. Lindberg, T. Earles, L. J. Mawst, and

Y. V. Flores, "High-efficiency, high-power mid-infrared quantum cascade lasers", *Opt. Mater. Express*, vol. 8, no. 5, pp. 1378–1398, 2018. DOI: 10.1364/OME.8.001378.

[9] A. Lyakh, R. Maulini, A. Tsekoun, R. Go, and C. K. N. Patel, "Multiwatt long wavelength quantum cascade lasers based on high strain composition with 70% injection efficiency", *Opt. Express*, vol. 20, no. 22, pp. 24 272–24 279, 2012. DOI: 10.1364/OE.20.024272.

[10] O. Cathabard, R. Teissier, J. Devenson, J. C. Moreno, and A. N. Baranov, "Quantum cascade lasers emitting near 2.6μm", *Applied Physics Letters*, vol. 96, no. 14, p. 141 110, 2010. DOI: 10.1063/1.3385778.

[11] M. S. Vitiello, G. Scalari, B. Williams, and P. D. Natale, "Quantum cascade lasers: 20 years of challenges", *Opt. Express*, vol. 23, no. 4, pp. 5167–5182, 2015. DOI: 10.1364/OE.23.005167.

[12] B. Schwarz, P. Reininger, H. Detz, T. Zederbauer, A. Maxwell Andrews, S. Kalchmair, W. Schrenk, O. Baumgartner, H. Kosina, and G. Strasser, "A bi-functional quantum cascade device for same-frequency lasing and detection", *Applied Physics Letters*, vol. 101, no. 19, 2012. DOI: 10.1063/1.4767128.

[13] P. M. Hundt, B. Tuzson, O. Aseev, C. Liu, P. Scheidegger, H. Looser, F. Kapsalidis, M. Shahmohammadi, J. Faist, and L. Emmenegger, "Multi-species trace gas sensing with dual-wavelength QCLs", *Applied Physics B: Lasers and Optics*, vol. 124, no. 6, pp. 1–9, 2018. DOI: 10.1007/s00340-018-6977-y.

[14] M. Jahjah, W. Ren, P. Stefański, R. Lewicki, J. Zhang, W. Jiang, J. Tarka, and F. K. Tittel, "A compact QCL based methane and nitrous oxide sensor for environmental and medical applications", *Analyst*, vol. 139, no. 9, pp. 2065–2069, 2014. DOI: 10.1039/c3an01452e.

[15] Y. Cao, N. P. Sanchez, W. Jiang, R. J. Griffin, F. Xie, L. C. Hughes, C.-e. Zah, and F. K. Tittel, "Simultaneous atmospheric nitrous oxide, methane and water vapor detection with a single continuous wave quantum cascade laser", *Optics Express*, vol. 23, no. 3, p. 2121, 2015. DOI: 10.1364/oe.23.002121.

[16] M. L. Silva, D. M. Sonnenfroh, D. I. Rosen, M. G. Allen, and A. O'Keefe, "Integrated cavity output spectroscopy measurements of nitric oxide levels in breath with a pulsed room-temperature quantum cascade laser", *Applied Physics B: Lasers and Optics*, vol. 81, no. 5, pp. 705–710, 2005. DOI: 10.1007/s00340-005-1922-2.

[17] L. Ciaffoni, G. Hancock, J. J. Harrison, J. P. H. Van Helden, C. E. Langley, R. Peverall, G. A. Ritchie, and S. Wood, "Demonstration of a mid-infrared cavity enhanced absorption spectrometer for breath acetone detection", *Analytical Chemistry*, vol. 85, no. 2, pp. 846–850, 2013. DOI: 10.1021/ac3031465.

[18] G. Wysocki, A. A. Kosterev, and F. K. Tittel, "Spectroscopic trace-gas sensor with rapidly scanned wavelengths of a pulsed quantum cascade laser for in situ NO monitoring of industrial exhaust systems", *Applied Physics B: Lasers and Optics*, vol. 80, no. 4-5, pp. 617–625, 2005. DOI: 10.1007/s00340-005-1764-y.

[19] T. Hieta and M. Merimaa, "Simultaneous detection of SO2, SO3 and H2O using QCL spectrometer for combustion applications", *Applied Physics B: Lasers and Optics*, vol. 117, no. 3, pp. 847–854, 2014. DOI: 10.1007/s00340-014-5896-9.

[20] J. Hildenbrand, J. Herbst, J. Wöllenstein, and A. Lambrecht, "Explosive detection using infrared laser spectroscopy", in *Quantum Sensing and Nanophotonic Devices VI*, M. Razeghi, R. Sudharsanan, and G. J. Brown, Eds., International Society for Optics and Photonics, vol. 7222, SPIE, 2009, pp. 84–95. DOI: 10.1117/12.808976.

[21] B. Hinkov, F. Fuchs, J. M. Kaster, Q. Yang, W. Bronner, R. Aidam, and K. Köhler, "Broad band tunable quantum cascade lasers for standoff detection of explosives", in *Proc.SPIE*, vol. 7484, 2009.

[22] H. Richter, M. Wienold, L. Schrottke, K. Biermann, H. T. Grahn, and H. W. Hubers, "4.7-THz Local Oscillator for the GREAT Heterodyne Spectrometer on SOFIA", *IEEE Transactions on Terahertz Science and Technology*, vol. 5, no. 4, pp. 539–545, 2015. DOI: 10.1109/TTHZ.2015.2442155.

[23] B. Schwarz, "Monolithic integration of mid-infrared photonics", PhD thesis, TU Wien, 2015.

[24] D. Ristanic, "Optoelectronics Integration: On-Chip Infrared Sensors", PhD thesis, TU Wien, 2015.

[25] W. Schmidt, "Absorptionsspektrophotometrie", in *Optische Spektroskopie*, John Wiley & Sons, Ltd, 2014, ch. 4, pp. 123–190. DOI: 10.1002/9783527663323.ch4.

[26] J. Faist, *Quantum cascade lasers*. Oxford: Oxford University Press, 2013.

[27] B. G. Lee, "Distributed Feedback Quantum Cascade Laser Arrays for Chemical Sensing", PhD thesis, Harvard University, 2008, pp. 1–128.

[28] Evans82, *Https://commons.wikimedia.org/w/index.php?curid=3408975*, 2008.

[29] J. Faist, F. Capasso, C. Sirtori, D. L. Sivco, A. L. Hutchinson, and A. Y. Cho, "Vertical transition quantum cascade laser with Bragg confined excited state", *Applied Physics Letters*, 1995. DOI: 10.1063/1.114005.

[30] M. Beck, D. Hofstetter, T. Aellen, J. Faist, U. Oesterle, M. Ilegems, E. Gini, and H. Melchior, "Continuous wave operation of a mid-infrared semiconductor laser at room temperature", *Science*, 2002. DOI: 10.1126/science.1066408.

[31] G. Scamarcio, F. Capasso, C. Sirtori, J. Faist, A. L. Hutchinson, D. L. Sivco, and A. Y. Cho, "High-power infrared (8-micrometer wavelength) superlattice lasers", *Science*, 1997. DOI: 10.1126/science.276.5313.773.

[32] J. Faist, M. Beck, T. Aellen, and E. Gini, "Quantum-cascade lasers based on a bound-to-continuum transition", *Applied Physics Letters*, 2001. DOI: 10.1063/1.1339843.

[33] A. Cho, *Molecular Beam Epitaxy*, ser. Key Papers in Applied Physics. Springer Verlag, 1994.

[34] F. Rinaldi, "Basics of Molecular Beam Epitaxy", *Annual Report*, p. 31, 2002.

[35] G. B. Stringfellow, "1 - Overview of the OMVPE Process", in *Organometallic Vapor-Phase Epitaxy (Second Edition)*, G. B. Stringfellow, Ed., Second Edi, San Diego: Academic Press, 1999, pp. 1–16. DOI: https://doi.org/10.1016/B978-012673842-1/50004-1.

[36] R. Pelzel, "A comparison of MOVPE and MBE growth technologies for III-V epitaxial structures", *2013 International Conference on Compound Semiconductor Manufacturing Technology, CS MANTECH 2013*, vol. C, no. 610, pp. 105–108, 2013.

[37] A. Czerwinski, M. Pluska, A. Łaszcz, J. Ratajczak, K. Piersciński, D. Pierscińska, P. Gutowski, P. Karbownik, and M. Bugajski, "Formation of coupled-cavities in quantum cascade lasers using focused ion beam milling", *Microelectronics Reliability*, vol. 55, no. 9-10, pp. 2142–2146, 2015. DOI: 10.1016/j.microrel.2015.06.111.

[38] C.-C. Hou, H.-M. Chen, J.-C. Zhang, N. Zhuo, Y.-Q. Huang, R. A. Hogg, D. T. Childs, J.-Q. Ning, Z.-G. Wang, F.-Q. Liu, and Z.-Y. Zhang, "Near-infrared and mid-infrared semiconductor broadband light emitters", *Light: Science & Applications*, vol. 7, no. 3, pp. 17 170–17 170, 2018. DOI: 10.1038/lsa.2017.170.

[39] R. Szedlak, J. Hayden, P. Martín-Mateos, M. Holzbauer, A. Harrer, B. Schwarz, B. Hinkov, D. MacFarland, T. Zederbauer, H. Detz, A. M. Andrews, W. Schrenk, P. Acedo, B. Lendl, and G. Strasser, "Surface emitting ring quantum cascade lasers for chemical sensing", *Optical Engineering*, vol. 57, no. 01, p. 1, 2017. DOI: 10.1117/1.oe.57.1.011005.

[40] M. Troccoli, L. Diehl, D. P. Bour, S. W. Corzine, N. Yu, C. Y. Wang, M. A. Belkin, G. Höfler, R. Lewicki, G. Wysocki, F. K. Tittel, and F. Capasso, "High-performance quantum cascade lasers grown by metal-organic vapor phase epitaxy and their applications to trace gas sensing", *Journal of Lightwave Technology*, vol. 26, no. 21, pp. 3534–3555, 2008. DOI: 10.1109/JLT.2008.925056.

[41] O. Wright, "Gallery of whispers", *Physics World*, vol. 25, no. 02, pp. 31–36, 2012. DOI: 10.1088/2058-7058/25/02/36.

[42] D. Hofstetter, M. Beck, and J. Faist, "Quantum-cascade-laser structures as photodetectors", *Applied Physics Letters*, vol. 81, no. 15, pp. 2683–2685, 2002. DOI: 10.1063/1.1512954.

[43] F. R. Giorgetta, E. Baumann, M. Graf, Q. Yang, C. Manz, K. Köhler, H. E. Beere, D. A. Ritchie, E. Linfield, A. G. Davies, Y. Fedoryshyn, H. Jäckel, M. Fischer, J. Faist, and D. Hofstetter, "Quantum cascade detectors", *IEEE Journal of Quantum Electronics*, vol. 45, no. 8, pp. 1039–1052, 2009. DOI: 10.1109/JQE.2009.2017929.

[44] A. Harrer, "Quantum Cascade Intersubband Devices for Mid-Infrared Sensing", PhD thesis, TU Wien, 2017.

[45] B. Schwarz, D. Ristanic, P. Reininger, T. Zederbauer, D. MacFarland, H. Detz, A. M. Andrews, W. Schrenk, and G. Strasser, "High performance bi-functional quantum cascade laser and detector", *Applied Physics Letters*, vol. 107, no. 7, 2015. DOI: 10.1063/1.4927851.

[46] B. Schwarz, C. A. Wang, L. Missaggia, T. S. Mansuripur, P. Chevalier, M. K. Connors, D. McNulty, J. Cederberg, G. Strasser, and F. Capasso, "Watt-Level Continuous-Wave Emission from a Bifunctional Quantum Cascade Laser/Detector", *ACS Photonics*, vol. 4, no. 5, pp. 1225–1231, 2017. DOI: 10.1021/acsphotonics.7b00133.

[47] B. Schwarz, P. Reininger, D. Ristanić, H. Detz, A. M. Andrews, W. Schrenk, and G. Strasser, "Monolithically integrated mid-infrared lab-on-a-chip using plasmonics and quantum cascade structures", *Nature Communications*, vol. 5, no. May, pp. 1–7, 2014. DOI: 10.1038/ncomms5085.

[48] R. Stanley, "Plasmonics in the mid-infrared", *Nature Photonics*, 2012. DOI: 10.1038/nphoton.2012.161.

[49] S. Franssila and L. Sainiemi, "Reactive Ion Etching (RIE)", in *Encyclopedia of Microfluidics and Nanofluidics*, D. Li, Ed., Boston, MA: Springer US, 2008, pp. 1772–1781. DOI: 10.1007/978-0-387-48998-8_1344.

[50] T. S. Cale, G. B. Raupp, B. R. Rogers, F. R. Myers, and T. E. Zirkle, "Introduction to Plasma Enhanced Chemical Vapor Deposition", in *Plasma Processing of Semiconductors*, P. F. Williams, Ed., Dordrecht:

Springer Netherlands, 1997, pp. 89–108. DOI: 10.1007/978-94-011-5884-8_5.

[51] L. Diehl, B. G. Lee, P. Behroozi, M. Loncar, M. Belkin, F. Capasso, T. Aellen, D. Hofstetter, M. Beck, and J. Faist, "Microfluidic tuning of distributed feedback quantum cascade lasers", *Optics Express*, vol. 14, no. 24, p. 11 660, 2006. DOI: 10.1364/oe.14.011660.

[52] U. K. Joachim Weiß, Marion Winkelbach, *Der Brockhaus — Naturwissenschaft und Technik, 1. Auflage (2003)*. F. A. Brockhaus, Spektrum Akademischer Verlag, 2003.

[53] G. A. Slack and C. J. Glassbrenner, "Thermal conductivity of Si and Ge from 3K to the melting point", *Physical Review*, vol. 134, no. 4A, A1058–A1069, 1964.

[54] S. M. Lee and D. G. Cahill, "Heat transport in thin dielectric films", *Journal of Applied Physics*, vol. 81, no. 6, pp. 2590–2595, 1997. DOI: 10.1063/1.363923.

[55] I. Kudman and E. F. Steigmeier, "Thermal conductivity and seebeck coefficient of InP", *Physical Review*, vol. 133, no. 6A, pp. 1665–1667, 1964. DOI: 10.1103/PhysRev.133.A1665.

[56] N. Chronis and L. P. Lee, "Electrothermally activated SU-8 microgripper for single cell manipulation in solution", *Journal of Microelectromechanical Systems*, vol. 14, no. 4, pp. 857–863, 2005. DOI: 10.1109/JMEMS.2005.845445.

[57] D. V. Land, A. P. Levick, and J. W. Hand, "The use of the Allan deviation for the measurement of the noise and drift performance of microwave radiometers", *Measurement Science and Technology*, vol. 18, no. 7, 2007. DOI: 10.1088/0957-0233/18/7/018.

[58] Y. Maréchal, "The molecular structure of liquid water delivered by absorption spectroscopy in the whole IR region completed with thermodynamics data", *Journal of Molecular Structure*, 2011. DOI: 10.1016/j.molstruc.2011.07.054.

[59] T. L. Myers, R. G. Tonkyn, A. M. Oeck, T. O. Danby, J. S. Loring, M. S. Taubmann, S. W. Sharpe, J. C. Birnbaum, and T. J. Johnson, "IARPA / PNNL Liquid Phase IR Spectra", in *NIST Chemistry WebBook, NIST Standard Reference Database Number 69*, Eds. P.J. Linstrom, W.G. Mallard, National Institute of Standards, and Technology, Gaithersburg MD, 20899, 2018. DOI: 10.18434/T4D303.

[60] A. Schwaighofer, M. R. Alcaraz, L. Lux, and B. Lendl, "pH titration of β-lactoglobulin monitored by laser-based Mid-IR transmission spectroscopy coupled to chemometric analysis", *Spectrochimica Acta - Part A: Molecular and Biomolecular Spectroscopy*, 2020. DOI: 10.1016/j.saa.2019.117636.

[61] M. R. Alcaráz, A. Schwaighofer, H. Goicoechea, and B. Lendl, "EC-QCL mid-IR transmission spectroscopy for monitoring dynamic changes of protein secondary structure in aqueous solution on the example of β-aggregation in alcohol-denaturated α-chymotrypsin", *Analytical and Bioanalytical Chemistry*, vol. 408, no. 15, pp. 3933–3941, 2016. DOI: 10.1007/s00216-016-9464-5.